



Metallicities and Refined Stellar Parameters for 52 Cool Dwarfs with Transiting Planets and Planet Candidates

Rebecca Gore^{1,2,3} , Steven Giacalone^{1,4,11} , Courtney D. Dressing¹ , Emma V. Turtelboom¹ , Ashley Schroeder^{1,5}, Charles D. Fortenbach⁶ , Kevin K. Hardegree-Ullman⁷ , Jon K. Zink^{4,12} , Andrew W. Mayo^{1,8} , Joshua E. Schlieder⁹ , and Jessie L. Christiansen¹⁰

¹ Department of Astronomy, University of California Berkeley, Berkeley, CA 94720, USA; giacalone@astro.caltech.edu

² Bay Area Environmental Research Institute, Moffett Field, CA 94035, USA

³ NASA Ames Research Center, Moffett Field, CA 94035, USA

⁴ Department of Astronomy, California Institute of Technology, Pasadena, CA 91125, USA

⁵ AstroCamp, Idyllwild, CA 92549, USA

⁶ Department of Physics and Astronomy, San Francisco State University, San Francisco, CA 94132, USA

⁷ Steward Observatory, The University of Arizona, Tucson, AZ 85721, USA

⁸ Centre for Star and Planet Formation, Natural History Museum of Denmark & Niels Bohr Institute, University of Copenhagen, Øster Voldgade 5-7, DK-1350 Copenhagen K., Denmark

⁹ NASA Goddard Space Flight Center, 8800 Greenbelt Rd., Greenbelt, MD 20771, USA

¹⁰ NASA Exoplanet Science Institute, IPAC, MS 100-22, Caltech, 1200 E. California Blvd., Pasadena, CA 91125, USA

Received 2023 December 22; revised 2024 February 14; accepted 2024 February 18; published 2024 March 28

Abstract

We collected near-infrared spectra of 65 cool stars with the NASA Infrared Telescope Facility and analyzed them to calculate accurate metallicities and stellar parameters. The sample of 55 M dwarfs and 10 K dwarfs includes 25 systems with confirmed planets and 27 systems with planet candidates identified by the K2 and TESS missions. Three of the 25 confirmed planetary systems host multiple confirmed planets and two of the 27 planet candidate systems host multiple planet candidates. Using the new stellar parameters, we refit the K2 and TESS light curves to calculate updated planet properties. In general, our updated stellar properties are more precise than those previously reported and our updated planet properties agree well with those in the literature. Lastly, we briefly examine the relationship between stellar mass, stellar metallicity, and planetary system properties for targets in our sample and for previously characterized planet-hosting low-mass stars. We provide our spectra, stellar parameters, and new planetary fits to the community, expanding the sample available with which to investigate correlations between stellar and planetary properties for low-mass stars.

Unified Astronomy Thesaurus concepts: Exoplanets (498); Exoplanet systems (484); Stellar properties (1624); M dwarf stars (982); Low mass stars (2050); Spectroscopy (1558)

Supporting material: machine-readable tables

1. Introduction

The Kepler and K2 missions discovered thousands of transiting planets in our Galaxy.¹³ While these missions were not primarily concerned with planets around M dwarfs (Borucki et al. 2010; Howell et al. 2014), they resulted in the discovery of hundreds of planets orbiting these cool stars (e.g., Morton et al. 2016). These discoveries have allowed for robust estimations of the occurrence rates of planets orbiting M dwarfs, specifically as a function of planet radius (R_p) and orbital period (P_{orb}) (e.g., Dressing & Charbonneau 2013, 2015; Muirhead et al. 2015; Mulders et al. 2015; Gaidos et al. 2016; Hardegree-Ullman et al. 2019; Bergsten et al. 2023). The number of known M dwarf planetary systems has increased even further with the Transiting Exoplanet Survey Satellite (TESS; Ricker et al. 2015), which can access low-mass stars more easily than Kepler due to its higher sensitivity at long

wavelengths. Some yield predictions projected the discovery of ≥ 1000 new transiting planets orbiting M dwarfs, most of which will be small ($R_p < 4 R_{\oplus}$) (Ballard 2019; Kunimoto et al. 2022). Others have found this prediction to be overoptimistic, and that TESS has delivered fewer small planets around cool stars than expected, possibly due to a low planet occurrence rate around the latest M dwarfs (Brady & Bean 2022). In either case, the sample of cool dwarf planets found by TESS will provide a foundation on which to more robustly explore correlations between the properties of cool stars and their planetary systems.

Using this new sample of planets, we can gain a better understanding of the relationship between planet occurrence rates and stellar metallicity. It has been shown that giant planets occur more frequently around more metal-rich FGK stars (e.g., Fischer & Valenti 2005; Johnson et al. 2010; Sousa et al. 2011). This correlation is more tenuous for M dwarfs, around which short-period giant planets are relatively rare and, due to the intrinsic faintness of low-mass stars, more challenging to find (e.g., Johnson & Apps 2009; Rojas-Ayala et al. 2012; Terrien et al. 2012; Gan et al. 2022, 2023a; Hartman et al. 2023). Several studies have searched for a link between stellar metallicity and the occurrence rate of smaller planets. Using a sample of several hundred planet-hosting stars, Buchhave et al. (2014) argued that stars hosting small ($R_p < 1.7 R_{\oplus}$) close-in planets have lower metallicities than those hosting close-in sub-

¹¹ NSF Astronomy and Astrophysics Postdoctoral Fellow.

¹² NHFP Sagan Fellow.

¹³ https://exoplanetarchive.ipac.caltech.edu/docs/counts_detail.html

Neptunes ($1.7 R_{\oplus} < R_p < 3.9 R_{\oplus}$) and gas giants ($R_p > 3.9 R_{\oplus}$), on average. Mulders et al. (2016) further explored this relationship by examining the connection between host-star metallicity and planet orbital period, finding that small planets with $P_{\text{orb}} < 10$ days orbit stars with higher metallicities than small planets with $P_{\text{orb}} > 10$ days. Petigura et al. (2018) analyzed the link between host-star metallicity and the frequency of small planets, concluding that they are equally common around metal-poor and metal-rich stars (also see Buchhave et al. 2012). These trends, or lack thereof, are most apparent for FGK stars, but have also been tentatively identified for M dwarfs (Rojas-Ayala et al. 2012; Neves et al. 2013; Hobson et al. 2018; Maldonado et al. 2020).

Some studies have also found evidence of correlations between stellar metallicity and system architecture. For instance, Brewer et al. (2018) showed that compact multiplanet systems are more commonly found around FGK stars that are metal-poor than those that are metal-rich (although we note that other studies find no such correlation; Weiss et al. 2018). Anderson et al. (2021) later found a similar trend as Brewer et al. (2018) for M dwarfs and late K dwarfs using Gaia color as a proxy for metallicity, showing that compact multiplanet systems tend to be around cool stars that are significantly bluer (more metal-poor) than stars hosting only a single planet. In an independent analysis that utilized planet-hosting M dwarfs with photometrically and spectroscopically determined metallicities, Rodríguez Martínez et al. (2023) also found a tendency for multiplanet systems to orbit more metal-poor M dwarfs than single-planet systems. As more planetary systems are discovered around these cool stars, having reliable metallicities will be crucial for similar population-level studies that aim to infer how this property influences planet formation and evolution around low-mass stars.

Our ability to measure the properties of M dwarfs has improved drastically over the last decade. In preparation for the K2 mission, the properties of cool stars were estimated primarily using broadband photometry and proper motions via the Galaxia galactic model (Sharma et al. 2011) and Padova isochrone models (Girardi et al. 2000; Marigo & Girardi 2007; Marigo et al. 2008), which were compiled in the Ecliptic Plane Input Catalog (EPIC; Huber et al. 2016). While the EPIC generally distinguishes cool dwarf stars from hotter stars, the documentation cautions that the stellar radius estimates could be systematically lower than the true values due to a tendency for the Padova models to underestimate the radii of cool dwarfs (Boyajian et al. 2012). This discrepancy poses a problem for studies of transiting planets around these stars, as underestimated stellar radii lead to underestimated planet radii for any transiting planets.

In the last decade, methods have been developed to circumvent this issue by using empirical relations to determine the physical properties of cool stars from parallax measurements and broadband photometry (e.g., Mann et al. 2013, 2014, 2015, 2019; Newton et al. 2014, 2015). These relations were leveraged in the curation of a cool dwarf list in the TESS Input Catalog (TIC; Muirhead et al. 2018; Stassun et al. 2018, 2019), which utilized the parallax measurements of millions of nearby M dwarfs in Gaia Data Release (DR) 2 (Gaia Collaboration et al. 2021). In addition, these relations made it possible to refine stellar parameters for M dwarfs by including measurements of stellar metallicity extracted from near-infrared spectra (e.g., Mann et al. 2013, 2014, 2015, 2019; Newton et al. 2014, 2015;

Terrien et al. 2015; Dressing et al. 2017; Martinez et al. 2017; Wittenmyer et al. 2018; Dressing et al. 2019).

In this paper we measure the metallicities of M dwarfs with transiting-planet candidates and confirmed transiting planets and use them to calculate refined stellar parameters. We then use these parameters to calculate updated radii and insolation fluxes for the planet candidates and planets. This work complements other surveys that have measured the metallicities of planet-hosting M dwarfs (e.g., Bean et al. 2006; Mann et al. 2012, 2013, 2014, 2015; Newton et al. 2014, 2015; Terrien et al. 2015; Dressing et al. 2017, 2019; Mann et al. 2019; Maldonado et al. 2020; Rains et al. 2021).

This paper is structured as follows. In Section 2, we describe the sample of stars characterized in this paper and the criteria used to select them. In Section 3, we discuss our observation strategy and data reduction procedure. In Section 4, we detail the process of extracting metallicities and improved stellar parameters from our spectra. In Section 5, we calculate updated orbital parameters and radii for the confirmed planets and planet candidates orbiting the stars in our sample. In Section 6, we explore the relationship between planetary system properties and stellar parameters in our sample and for previously characterized low-mass stars. Lastly, in Section 7, we provide concluding remarks.

2. Target Selection

The goal of this paper is to calculate the metallicities and update stellar parameters for M dwarfs and late K dwarfs (M5–K7) with transiting planets and planet candidates. Accordingly, we selected targets to observe based on the following criteria: (1) the star must have either a transiting-planet candidate or a known transiting planet, (2) the star must have an estimated effective temperature (T_{eff}) less than 5300 K and a surface gravity ($\log g$) greater than 4.0 according to the EPIC (Huber et al. 2014) or version 8.2 of the TIC (Stassun et al. 2018, 2019; with a preference for lower values of T_{eff} and higher values of $\log g$), and (3) the star must be observable from the Infrared Telescope Facility (IRTF) (that is, it must have a decl. between 70° and -59°). In addition, we prioritized brighter stars that allowed us to acquire higher signal-to-noise (S/N) spectra as well as stars that seem scientifically compelling, either because they already had a confirmed planet or had a promising planet candidate. Lastly, we consulted the IRTF Data Archive¹⁴ to verify that each target did not already have IRTF/SpeX data from earlier large-scale cool-star surveys (e.g., Newton et al. 2014; Terrien et al. 2015). We also observed a small number of cool stars that are not flagged as having transiting-planet candidates for the purpose of compiling a set of “control” stars with which to compare the properties of planet-hosting stars. We note that stars within the control sample are statistically likely to harbor planets in nontransiting geometries or planets that were not detectable in transit given the existing TESS and K2 data. We include these stars in our analyses, as they may be of interest to future studies.

Our complete target sample, which consists of 65 stars, is presented in Table 1. This table includes a number of stellar properties from various catalogs that we recalculate in Section 4.3. The two rightmost columns of the table indicate whether the objects of interest around the stars are planet candidates, confirmed planets, or false positives, as well as the

¹⁴ <https://irsa.ipac.caltech.edu/applications/irtf/>

Table 1
Initial Properties of the 65 Systems in This Work

ID	Alt. Name	Campaign/Sector	V	J	K_s	d (pc)	R_* (R_\odot)	M_* (M_\odot)	$\log g$ (dex)	T_{eff} (K)	Sp. T.	S/N	Disp.	Date
EPIC 211510580	...	5,18	16.34	12.48	11.63	99.70 ± 0.30	0.36 ± 0.19	0.39 ± 0.21	4.920 ± 0.020	3855 ± 431	M2.5 V	130	PC	...
EPIC 211586387	...	5,16,18	14.64	12.70	12.04	323.62 ± 2.09	0.67 ± 0.04	0.74 ± 0.05	4.647 ± 0.036	4660 ± 111	K2 V	133	PC	...
EPIC 211663688	...	16	19.11	14.12	13.25	99.80 ± 0.80	0.32 ± 0.09	0.34 ± 0.13	4.942 ± 0.102	3768 ± 221	M4.5 V	47	PC	...
EPIC 211673349	...	16	14.76	12.65	11.90	305.81 ± 1.87	0.53 ± 0.07	0.59 ± 0.09	4.754 ± 0.064	4245 ± 83	K4 V	159	PC	...
EPIC 211731298	...	5,18	13.20	11.73	11.23	285.71 ± 1.63	0.78 ± 0.06	0.86 ± 0.05	4.571 ± 0.020	5244 ± 83	K2 V	169	PC	...
EPIC 211863149	...	16	15.89	12.18	11.27	117.23 ± 0.41	0.32 ± 0.07	0.34 ± 0.09	4.956 ± 0.078	3730 ± 175	M2.5 V	154	PC	...
EPIC 211925595	...	5,16	14.58	13.02	12.43	478.47 ± 4.58	0.72 ± 0.05	0.79 ± 0.05	4.612 ± 0.030	4874 ± 77	K2 V	133	PC	...
EPIC 212048748	K2-313	16	13.82	10.06	9.19	27.83 ± 0.02	0.31 ± 0.04	0.33 ± 0.05	4.964 ± 0.049	3713 ± 129	M2.5 V	211	CP	2020-03
EPIC 212088059	K2-345	5,16,18	15.72	12.34	11.46	161.55 ± 0.52	0.40 ± 0.08	0.45 ± 0.10	4.877 ± 0.072	3852 ± 136	M1 V	159	CP	2021-11
EPIC 248433930	...	14	14.45	11.54	10.72	115.87 ± 0.27	0.38 ± 0.08	0.43 ± 0.11	4.903 ± 0.080	3829 ± 122	M1 V	109
EPIC 248440276	...	14	14.60	10.93	10.08	57.08 ± 0.07	0.24 ± 0.04	0.23 ± 0.06	5.042 ± 0.050	3525 ± 69	M2.5 V	184
EPIC 248527514	K2-401	14	14.01	11.87	11.11	201.61 ± 0.81	0.40 ± 0.13	0.45 ± 0.14	4.878 ± 0.128	4200 ± 149	K5 V	165	CP	2022-06
EPIC 248731669	...	14	16.57	13.38	12.52	261.78 ± 3.43	0.31 ± 0.08	0.35 ± 0.10	4.966 ± 0.088	3750 ± 175	M0.5 V	102
EPIC 248775938	...	14	15.88	13.09	12.20	311.53 ± 3.88	0.46 ± 0.05	0.53 ± 0.06	4.817 ± 0.048	4018 ± 96	M0.5 V	133	PC	...
EPIC 248856002	...	14	16.00	13.07	12.15	189.04 ± 1.43	0.28 ± 0.08	0.29 ± 0.10	5.014 ± 0.096	3663 ± 128	M2 V	140
EPIC 248861279	K2-404	14	14.62	11.58	10.75	121.65 ± 0.30	0.35 ± 0.05	0.39 ± 0.06	4.928 ± 0.048	3775 ± 60	M1 V	161	CP	2022-06
TIC 2760710	TOI-227	2,29	18.44	12.13	11.25	52.63 ± 0.11	0.24 ± 0.01	0.21 ± 0.02	4.998 ± 0.014	3176 ± 157	M4.5 V	116	PC	...
TIC 415969908	TOI-233	2,29,43	13.34	9.94	9.09	33.73 ± 0.02	0.38 ± 0.01	0.37 ± 0.02	4.845 ± 0.002	3568 ± 157	M2.5 V	165	2×PC	...
TIC 12423815	TOI-234	2,29	16.52	13.22	12.33	253.16 ± 2.56	0.55 ± 0.02	0.54 ± 0.02	4.695 ± 0.011	3628 ± 157	M0.5 V	98	PC	...
TIC 118327550	TOI-244	2,29	12.86	8.83	7.97	22.08 ± 0.01	0.41 ± 0.01	0.40 ± 0.02	4.820 ± 0.004	3407 ± 157	M2.5 V	70	CP	2023-07
TIC 120916706	TOI-263	3,4,30	18.97	14.08	13.25	286.53 ± 5.75	0.44 ± 0.02	0.44 ± 0.02	4.791 ± 0.010	3423 ± 157	M3 V	58	FP	2021-03
TIC 70899085	TOI-442	5,32	12.49	9.49	8.63	52.33 ± 0.05	0.61 ± 0.02	0.59 ± 0.02	4.645 ± 0.011	3779 ± 157	M1 V	207	CP	2020-12
TIC 365639282	TOI-482	6,32	14.94	11.74	10.95	143.06 ± 4.09	0.56 ± 0.02	0.56 ± 0.02	4.684 ± 0.011	3692 ± 157	M2.5 V	126	FP	2019-11
TIC 452866790	TOI-488	7,34,61	13.74	9.63	8.83	27.31 ± 0.01	0.35 ± 0.01	0.34 ± 0.02	4.870 ± 0.001	3329 ± 157	M3.5 V	201	2×CP	2020-10
TIC 19025965	TOI-493	7,34,44–46,61	12.55	10.36	9.63	107.41 ± 0.23	0.81 ± 0.07	0.65 ± 0.03	4.431 ± 0.098	4139 ± 106	M0 V	216	PC	...
TIC 348538431	TOI-507	7,34,61	16.30	11.65	10.84	109.89 ± 0.24	0.51 ± 0.02	0.50 ± 0.02	4.733 ± 0.009	3330 ± 157	M4 V	159	PC	...
TIC 318937509	TOI-516	7	17.20	12.36	11.49	152.67 ± 0.93	0.51 ± 0.02	0.50 ± 0.02	4.732 ± 0.009	3225 ± 157	M0.5 V	101	FP	2020-11
TIC 218795833	TOI-519	7,8,34	17.35	12.85	11.95	115.21 ± 0.53	0.36 ± 0.01	0.34 ± 0.02	4.869 ± 0.001	3324 ± 157	M2.5 V	102	CP	2023-08
TIC 27649847	TOI-521	7,34,44–46,61	14.69	10.92	10.09	61.01 ± 0.07	0.42 ± 0.01	0.41 ± 0.02	4.808 ± 0.005	3465 ± 157	M2 V	270	PC	...
TIC 93125144	TOI-523	6,32,33	10.71	8.74	8.12	69.93 ± 0.83	0.89 ± 0.05	0.79 ± 0.09	4.434 ± 0.065	4852 ± 121	K2 V	219	FP	2021-03
TIC 200593988	TOI-526	6	14.31	10.92	10.11	70.87 ± 0.10	0.47 ± 0.01	0.46 ± 0.02	4.767 ± 0.007	3601 ± 157	M1.5 V	447	FP	2022-10
TIC 387690507	TOI-530	6,33,44,45	15.40	12.11	11.24	147.71 ± 0.65	0.54 ± 0.02	0.54 ± 0.02	4.698 ± 0.010	3566 ± 157	M1 V	114	CP	2022-03
TIC 144700903	TOI-532	6	14.41	11.47	10.59	135.32 ± 0.37	0.62 ± 0.02	0.61 ± 0.02	4.631 ± 0.011	3815 ± 157	M0 V	126	CP	2021-10
TIC 237751146	TOI-538	6,33	16.54	12.62	11.70	134.23 ± 0.90	0.43 ± 0.01	0.43 ± 0.02	4.796 ± 0.006	3352 ± 157	M3 V	99	FP	2021-02
TIC 50618703	TOI-544	6,32	10.78	8.59	7.80	40.92 ± 0.03	0.66 ± 0.06	0.66 ± 0.08	4.614 ± 0.110	4220 ± 123	K7 V	244	CP	2022-02
TIC 192826603	TOI-551	5,6,32,33	15.67	12.70	11.94	217.86 ± 0.95	0.57 ± 0.02	0.56 ± 0.02	4.679 ± 0.010	3902 ± 157	M0.5 V	109	CP	2018-04
TIC 170849515	TOI-555	5,31,32	16.68	13.69	12.81	395.26 ± 4.69	0.63 ± 0.02	0.61 ± 0.02	4.623 ± 0.013	3929 ± 157	M1.5 V	78	CP	2022-03
TIC 55488511	TOI-557	5,31	13.34	10.41	9.61	75.47 ± 0.11	0.57 ± 0.02	0.57 ± 0.02	4.673 ± 0.010	3841 ± 157	K7 V	178	PC	...
TIC 101011575	TOI-560	8,34,61	9.67	7.65	6.95	31.59 ± 0.02	0.63 ± 0.05	0.75 ± 0.09	4.714 ± 0.010	4695 ± 138	K2 V	299	2×CP	2022-08
TIC 413248763	TOI-562	8,35,62	10.91	7.34	6.47	9.436 ± 0.002	0.36 ± 0.01	0.35 ± 0.02	4.864 ± 0.001	3490 ± 157	M2 V	323	3×CP	2019-08
TIC 1133072	TOI-566	8,34,35,61,62	15.34	11.17	10.28	84.18 ± 0.14	0.50 ± 0.01	0.49 ± 0.02	4.741 ± 0.008	3471 ± 157	M2.5 V	110	FP	2019-04
TIC 296780789	TOI-573	8,35,62	15.02	11.11	10.23	88.73 ± 0.16	0.34 ± 0.06	0.34 ± 0.07	4.911 ± 0.395	...	M2 V	70	PC	...
TIC 296739893	TOI-620	8,35,62	12.26	8.84	7.95	33.01 ± 0.03	0.55 ± 0.02	0.54 ± 0.02	4.696 ± 0.010	3586 ± 157	M2.5 V	113	CP	2022-06
TIC 32497972	TOI-876	5,6,32,33	13.18	10.33	9.51	78.06 ± 0.06	0.60 ± 0.02	0.59 ± 0.02	4.648 ± 0.011	3882 ± 157	M0.5 V	157	PC	...
TIC 29960110	TOI-1201	4,31	12.26	9.53	8.65	37.63 ± 0.02	0.48 ± 0.01	0.48 ± 0.02	4.753 ± 0.008	3506 ± 157	M2 V	246	CP	2021-12
TIC 163539739	TOI-1278	15,55,56	13.40	10.60	9.73	75.47 ± 0.06	0.55 ± 0.02	0.55 ± 0.02	4.694 ± 0.009	3841 ± 157	M0.5V	164	CP	2021-10
TIC 13684720	TOI-1433	14,15,41,55	15.60	10.81	9.95	68.07 ± 0.05	0.48 ± 0.01	0.47 ± 0.02	4.758 ± 0.007	3275 ± 157	M3 V	159	PC	...

Table 1
(Continued)

ID	Alt. Name	Campaign/Sector	V	J	K _s	d (pc)	R _* (R _⊕)	M _* (M _⊕)	log g (dex)	T _{eff} (K)	Sp. T.	S/N	Disp.	Date
TIC 343628284	TOI-1448	15–17,57	15.68	11.60	10.77	73.64 ± 0.05	0.38 ± 0.01	0.37 ± 0.02	4.844 ± 0.002	3391 ± 157	M3 V	133	PC	...
TIC 240968774	TOI-1467	17,18,58	12.29	9.38	8.57	37.52 ± 0.03	0.49 ± 0.01	0.49 ± 0.02	4.746 ± 0.008	3834 ± 157	M2 V	233	PC	...
TIC 243185500	TOI-1468	17,42,43,57	12.50	9.34	8.50	24.72 ± 0.02	0.37 ± 0.01	0.36 ± 0.02	4.855 ± 0.001	3382 ± 157	M3.5 V	132	2×CP	2022-10
TIC 201186294	TOI-1634	18	13.22	9.48	8.60	35.08 ± 0.02	0.47 ± 0.01	0.46 ± 0.02	4.768 ± 0.007	3455 ± 157	M3 V	131	CP	2021-08
TIC 348673213	TOI-1639	18,58	14.38	11.78	10.94	154.08 ± 0.47	0.61 ± 0.02	0.60 ± 0.02	4.642 ± 0.011	3896 ± 157	M0.5 V	150	FP	2021-08
TIC 28900646	TOI-1685	19,59	13.38	9.62	8.76	37.61 ± 0.03	0.46 ± 0.01	0.46 ± 0.02	4.771 ± 0.007	3457 ± 157	M2 V	248	CP	2021-06
TIC 353475866	TOI-1693	19,43–45	12.96	9.19	8.33	30.85 ± 0.02	0.46 ± 0.01	0.46 ± 0.02	4.772 ± 0.007	3474 ± 157	M2.5 V	260	CP	2022-02
TIC 470381900	TOI-1696	19,59	16.82	12.23	11.33	64.60 ± 0.12	0.28 ± 0.01	0.25 ± 0.02	4.948 ± 0.008	3181 ± 157	M4.5 V	129	CP	2022-06
TIC 318022259	TOI-1730	20,47,60	12.23	9.06	8.21	35.65 ± 0.03	0.53 ± 0.02	0.53 ± 0.02	4.709 ± 0.009	3691 ± 157	M0.5 V	260	3 × PC	...
TIC 104208182	TOI-1738	18,19	14.07	11.31	10.46	141.84 ± 0.40	0.67 ± 0.02	0.64 ± 0.02	4.594 ± 0.012	3948 ± 157	M0 V	189	PC	...
TIC 408636441	TOI-1759	16,17,24,56–58	11.93	8.77	7.93	40.13 ± 0.02	0.63 ± 0.02	0.61 ± 0.02	4.629 ± 0.011	3960 ± 157	M2 V	200	CP	2022-03
TIC 389900760	TOI-2120	18,24,25,52,58	15.65	11.10	10.21	32.19 ± 0.02	0.24 ± 0.01	0.21 ± 0.02	5.000 ± 0.015	3179 ± 157	M4.5 V	164	PC	...
TIC 329148988	TOI-2285	16,17,24,56,57	13.40	9.86	9.03	42.48 ± 0.04	0.46 ± 0.01	0.46 ± 0.02	4.773 ± 0.007	3546 ± 157	M2 V	205	CP	2022-02
TIC 321688498	TOI-2290	17,18,24,25,57,58	12.64	9.90	9.07	58.11 ± 0.03	0.57 ± 0.02	0.56 ± 0.02	4.680 ± 0.010	3863 ± 157	M0.5 V	147	PC	...
TIC 168751223	TOI-2331	4,5,31	15.08	12.13	11.28	162.07 ± 0.53	0.57 ± 0.02	0.57 ± 0.02	4.674 ± 0.011	3798 ± 157	M0.5V	110	PC	...
TIC 212957629	TOI-2406	3,30,42,43	17.30	12.63	11.89	55.62 ± 0.12	0.20 ± 0.01	0.17 ± 0.02	5.070 ± 0.026	3163 ± 157	M4 V	137	CP	2021-09
TIC 350043412	TOI-5131	45,46	14.28	12.03	11.27	216.92 ± 0.94	0.63 ± 0.03	0.69 ± 0.08	4.674 ± 0.069	4427 ± 122	K3 V	183	PC	...
TIC 330637910	TOI-5561	44,45,46	17.53	13.74	12.88	272.48 ± 4.45	0.49 ± 0.02	0.49 ± 0.02	4.746 ± 0.017	3449 ± 157	M2.5 V	99	PC	...

Note. Columns from left to right are as follows: the EPIC or TIC ID of the star (Huber et al. 2014; Stassun et al. 2018, 2019); the alternative identifier of the star; the K2 or TESS sectors in which the star was observed; the V magnitude according to the TIC; the J and K_s magnitudes according to 2MASS (Skrutskie et al. 2006); Gaia DR3 distance of the star (Gaia Collaboration et al. 2023); the stellar radius, mass, surface gravity, and effective temperature according to the EPIC or TIC; the best-fit spectral type of the star from our spectrum (see Section 4.3); the maximum S/N of our spectrum of the star; a flag indicating the number and current status (as of the writing of this paper) of planet candidates around the star according to the NASA Exoplanet Archive and ExoFOP (where CP = confirmed planet, PC = planet candidate, and FP = false positive); and the year and month that the planet candidates were determined to be confirmed planets (i.e., the publication date of the discovery paper) or false positives (which is listed on ExoFOP). TOI-523 and TOI-5131 did not have uncertainties for R_{*} or M_{*} in the TIC. The uncertainties for those two targets were calculated manually using the relations defined in Section 2.3.5 of Stassun et al. (2019).

(This table is available in machine-readable form.)

dates on which these objects were classified as such. These flags and dates are based on information in the NASA Exoplanet Archive (NASA Exoplanet Science Institute 2020) and ExoFOP (ExoFOP 2019). We adopted the following key for labeling planetary systems

1. CP: The star hosts one or more confirmed planets.
2. PC: The star hosts at least one planet candidate but does not host confirmed planets.
3. FP: The star was previously reported to host a planet candidate that was later determined to be a false positive.

We note that TIC 163539739 (TOI-1278) is labeled as CP but actually hosts a transiting brown dwarf ($M = 18.5 \pm 0.5 M_J$; Artigau et al. 2021), but we choose to keep it in our analysis due to the rarity of these objects (e.g., Grether & Lineweaver 2006; Sahlmann et al. 2011). Planet candidates and confirmed planets orbiting stars in our sample are discussed further in Sections 5 and 6.

3. Observations

Our observing procedure follows that used in similar previous studies (e.g., Dressing et al. 2017, 2019). We observed our targets with the SpeX spectrograph on the 3 m NASA IRTF. Our observations were acquired during the 2018B–2020B semesters under programs 2018B112 (PI: Dressing), 2019A072 (PI: Dressing), and 2020B115 (PI: Giacalone). We collected our observations in short wavelength cross-dispersed mode with a $0.^{\prime\prime}3 \times 15.^{\prime\prime}$ slit, providing a spectral resolution of $R \approx 2000$ over a wavelength range of 0.7–2.55 μm (Rayner et al. 2003, 2004). We experienced subarcsecond seeing on all nights of observation.

All of our observations were collected using an ABBA nod pattern, with the A and B positions located $7.^{\prime\prime}5$ apart, in order to remove telescope and sky backgrounds. We also synced the slit to the parallactic angle in all cases to ensure that atmospheric dispersion occurred along the slit (minimizing light loss) and to reduce systematics that could affect the measured spectral shapes of our targets. The ABBA nod pattern was repeated with the goal of achieving an S/N of at least 100 per resolution element. The measured S/N of each spectrum is listed in Table 1.

In addition to our science targets, we acquired observations of A0V stars to use for telluric correction (Vacca et al. 2003). These A0V stars were observed within 1 hr of our science targets and had angular distances and airmass differences no greater than 15° and 0.1, respectively.

Lastly, we obtained calibrations throughout the night using internal quartz and thorium–argon lamps. Because SpeX is physically attached to the telescope, we ran a new calibration sequence every time we moved to a new part of the sky to account for systematics stemming from telescope pointing.

We reduced our spectra using the Spextool reduction pipeline (Cushing et al. 2004). Telluric contamination in our spectra was removed using our data of A0V stars and `xstellcor` (Vacca et al. 2003), a tool included within Spextool.

4. Data Analysis and Stellar Characterization

4.1. Initial Classification

In a similar manner as Dressing et al. (2017, 2019), we started our analysis by performing an initial classification of

our targets based on their spectra. For each star, we first split the spectrum into three segments corresponding to the J , H , and K_s passbands and mean normalized each. We then did the same for all stars in the IRTF Spectral Library with M, K, and G spectral types (Rayner et al. 2009). After correcting for differences in radial velocity, we calculated the χ^2 between the target spectrum and each library spectrum in each passband separately, identifying the library spectrum that provides the best fit at each range of wavelengths. For stars where all passbands agreed on the best-fit library spectrum, we assigned the corresponding spectral type. For stars where different passbands preferred different spectral types, we visually inspected the full spectra to determine which library spectrum provided the best match. We believe this method to provide spectral types that are accurate to within one subtype. We show the results of this analysis in Table 1 and visualize the comparison in Figure 1.

4.2. Identifying Possible Stellar Binaries

Before performing a detailed analysis of our targets to determine their metallicities and stellar properties, we sought to determine if any of our targets have nearby ($<2''$) stellar companions. Identifying these companions is important because their point-spread functions are typically blended with the primary star, causing them to influence the spectra and apparent magnitudes of the sources. As a result, they can affect the stellar parameters that we extract from the data and lead to erroneous results (see Section 4.3).

First, we searched for known stellar companions by querying Gaia DR3 in a $2''$ cone around each star. For TIC 296780789, we identified the nearby star TIC 876200725 ($\Delta T = 2.10$, $\Delta G = 0.85$, $\text{sep} = 1.^{\prime\prime}33$, $\text{PA} = 123^{\circ}$ east of north, where PA is position angle).¹⁵ The two stars share similar parallaxes ($\pi = 11.27 \text{ mas}$ and $\pi = 11.23 \text{ mas}$, respectively) and proper motions ($\text{pmra} = -51.68 \text{ mas yr}^{-1}$ and $\text{pmdec} = -92.24 \text{ mas yr}^{-1}$ for TIC 296780789, $\text{pmra} = -46.98 \text{ mas yr}^{-1}$ and $\text{pmdec} = -95.18 \text{ mas yr}^{-1}$ for TIC 876200725), indicating that the two stars are likely gravitationally bound. In addition, for TIC 348673213, we identified the nearby star TIC 624816660 ($\Delta T = 4.83$, $\Delta G = 4.31$, $\text{sep} = 1.^{\prime\prime}80$, $\text{PA} = 184^{\circ}$ east of north). These two stars do not share close parallaxes or proper motions, meaning they are most likely chance aligned. We note that TIC 296780789 is listed as having an “ambiguous” planet candidate on ExoFOP, indicating that it will be difficult to determine if the planet is real due to the presence of the nearby star and has a relatively high chance of being a false positive, and TIC 348673213 is listed as being a false positive. Due to the presence of the blended stars, we remove both of these targets from further analysis.

Next, we searched for evidence of binary stars that are unresolved by Gaia photometry. To do this, we queried Gaia DR3 and determined the renormalized unit weight error (RUWE) for each star. RUWE is known as a useful metric for binarity, where stars with $\text{RUWE} > 1.4$ are significantly more likely to be members of unresolved binary systems than those with smaller values (Lindegren et al. 2018; Belokurov et al. 2020; El-Badry et al. 2021). We identified only two stars in our sample with high RUWE: TIC 365639282 (RUWE = 10.50) and TIC 93125144 (RUWE = 12.56). As

¹⁵ Here, T is TESS magnitude and G is Gaia magnitude.

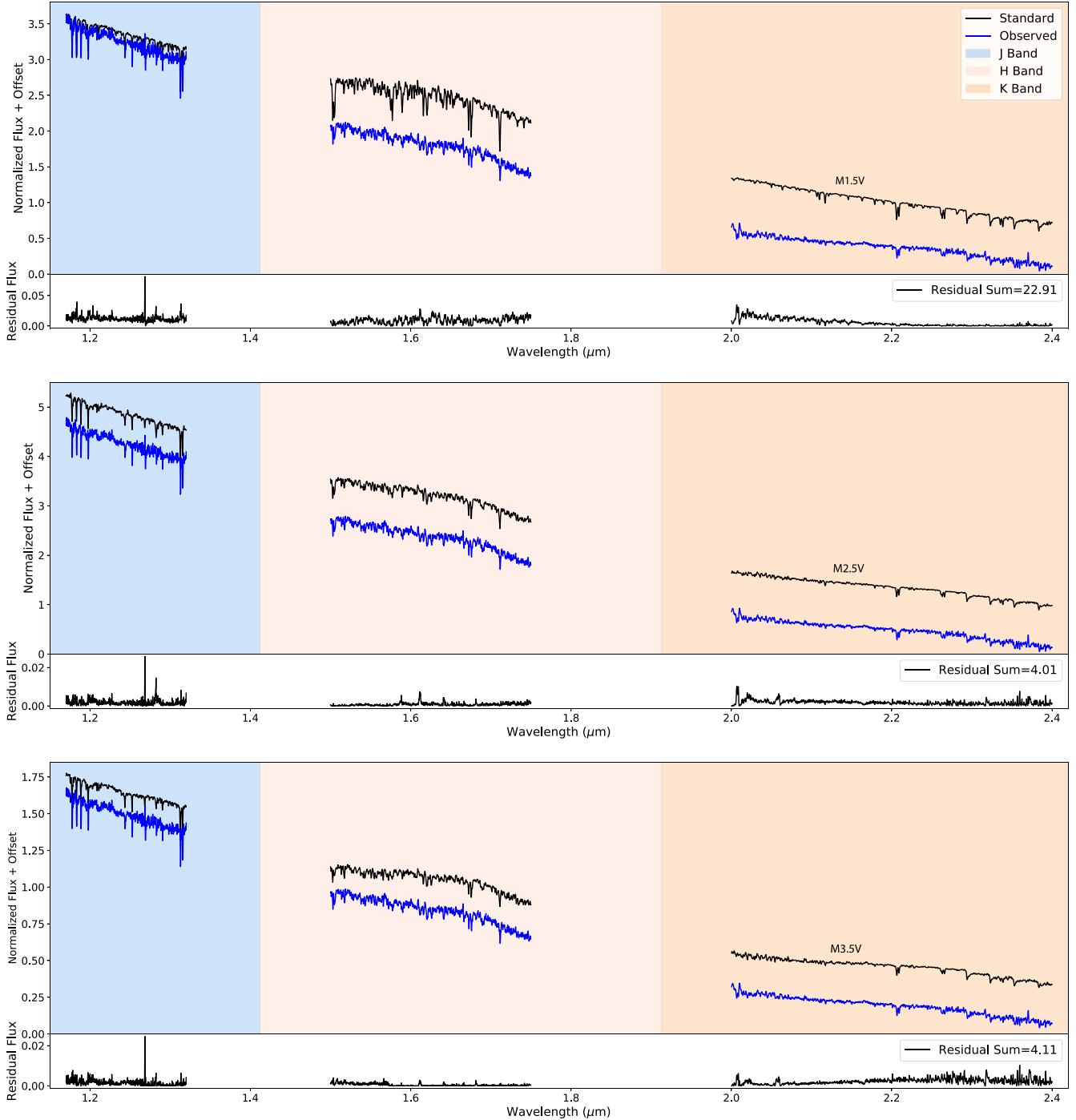


Figure 1. The observed spectrum for EPIC 212048748 compared with the IRTF standard spectrum (offset vertically for visual clarity) of HD 36395 (M1.5V; top) Gl 381 (M2.5V; middle), Gl 273 (M3.5V; bottom) within the highlighted *J*, *H*, and *K* bands. The bottom panels display the residuals between the observed and standard spectra, with Gl 381 providing the best match to the data. Data strongly influenced by telluric contamination has been masked out.

we note in Table 1, the TOIs associated with both of these stars have already been designated as false positives. We removed these targets from further analysis. After this vetting step, our sample contained 61 stars.

4.3. Detailed Classification

After our initial classification and removing probable binaries, we performed a more detailed analysis to extract metallicities from our spectra and calculate updated stellar parameters. We began by shifting our spectra into the lab frame

using `tellrv`, a code that measures absolute radial velocities of stars using near-infrared spectra (Newton et al. 2014, 2022).¹⁶ For the analysis in this paper, we converted the code from its native `IDL` to Python, which we have made available on GitHub.¹⁷ In short, the code works by wavelength calibrating the spectrum of the target star using telluric features in the near-infrared and then cross correlating it with a standard star with a known radial velocity. All of our lab-frame spectra

¹⁶ <https://github.com/ernewton/tellrv>

¹⁷ <https://github.com/stevengiacalone/tellrv>

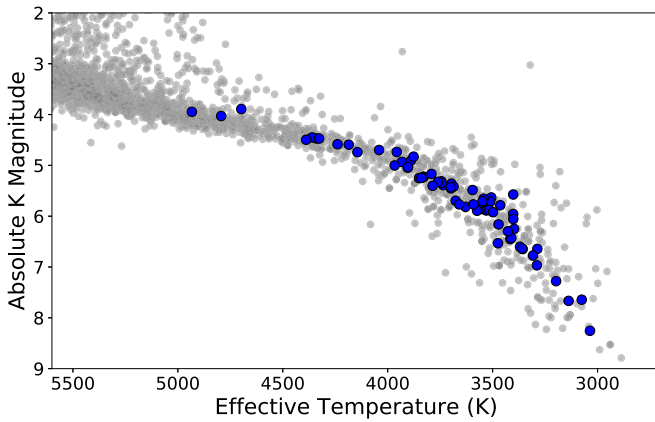


Figure 2. Hertzsprung–Russell diagram using the updated values of our observed stars from Section 4 (blue circles). For reference, all TESS Objects of Interest are plotted in the background (gray circles).

are publicly available and can be downloaded on ExoFOP.¹⁸ After this correction, we calculated the metallicities and updated stellar parameters for each of our targets using the following methods.

4.3.1. Spectrum-derived Stellar Metallicities

Using our lab-frame spectra, we calculated metallicities ($[Fe/H]$ and $[M/H]$) using the relations defined in Mann et al. (2013), which are valid for cool dwarfs with spectral types between K7 and M5. As is shown in Table 1, some of the stars observed fall outside of this spectral type range according to our initial classification: EPIC 211586387 (K2 V), EPIC 211673349 (K4 V), EPIC 211731298 (K2 V), EPIC 211925595 (K2 V), EPIC 248527514 (K2-401; K5 V), TIC 101011575 (TOI-560; K2 V), and TIC 350043412 (TOI-5131; K3 V). We removed these stars from further analysis to avoid reporting erroneous metallicities and stellar parameters. The Mann et al. (2013) relations allow for the calculation of metallicity across several passbands, but Dressing et al. (2019) reported metallicities derived using the K_s band to be the most reliable in spectra collected with SpeX, likely due to a lower level of contamination from tellurics compared to the H band. We therefore adopt values of $[Fe/H]$ and $[M/H]$ derived from the K_s -band spectra, adding a systematic uncertainty of 0.08 dex in quadrature with the uncertainties returned by the Mann et al. (2013) relations, as is recommended in the header of the code on GitHub.¹⁹ We report these metallicities in Table 2.

4.3.2. Gaia-derived Stellar Properties

We calculated updated stellar parameters using a combination of methods. First, we calculated the absolute J and K_s magnitudes (M_J and M_{K_s} , respectively) of each star using stellar parallaxes reported in Gaia DR3 (Gaia Collaboration et al. 2023), propagating uncertainties based on those reported by the Two Micron All Sky Survey (2MASS) and Gaia. Next, we used the metallicity-dependent relation in Table 3 of Mann et al. (2015) to calculate the $V-J$ bolometric correction. We calculated uncertainties for the bolometric correction using the uncertainties in V and J reported in the TIC and 2MASS and the uncertainties in $[Fe/H]$ calculated above, subsequently

adding a systematic uncertainty of 0.012 in quadrature as recommended in Mann et al. (2015). We then used the correction and M_J to calculate the absolute bolometric magnitude and bolometric luminosity (L_*) of each star. Next, we calculated values of R_* following the $R_*-M_{K_s}-[Fe/H]$ relation in Equation (5) and Table 1 of Mann et al. (2015). We calculated uncertainties in R_* using those previously calculated for M_{K_s} and $[Fe/H]$, subsequently adding a systematic fractional uncertainty of 2.7% in quadrature. We continued by calculating values of M_* using the fifth-order $M_*-M_{K_s}$ relation defined in Table 6 of Mann et al. (2019). We calculated uncertainties in M_* using those previously calculated for M_{K_s} , subsequently adding a systematic uncertainty of $0.02 M_\odot$ in quadrature as recommended in Mann et al. (2019). Similar to Dressing et al. (2019), we opted to not use the metallicity-dependent relations in Mann et al. (2019) to calculate M_* , due to the current small sample of M dwarfs with precisely constrained masses. Lastly, we calculated T_{eff} using the Stefan–Boltzmann relation. Our full set of updated parameters is shown in Table 2. For illustrative purposes, we show in Figure 2 the locations of our targets on the Hertzsprung–Russell diagram using our updated stellar parameters. All stars in our sample lie within the main-sequence track, supporting the notion that they host bona fide planets rather than false positives caused by blended companion stars. Our updated parameters are compared to their respective catalog parameters in Figure 3, demonstrating that our stellar properties provide a significant improvement over those reported in the EPIC²⁰ and are generally consistent with (although often more precise than) those in the TIC.

5. Updated Planet Parameters

Using our new stellar parameters, we performed light-curve fits for all of the stars in our sample with confirmed planets and planet candidates to calculate updated planet radii and orbital properties. All targets listed as CP and PC in Table 1 are included in these calculations with the exception of those removed from the analysis in the previous section. We also exclude EPIC 211663688 and EPIC 211863149 (Yu et al. 2018), as we were unable to recover the reported transits of their planet candidates in the K2 light curves.²¹ Our new best-fit planet parameters are displayed in Tables 3 and 4. We describe our calculation procedure below.

5.1. Light-curve Generation

We obtained the light curves for the confirmed planets in our sample using the Lightkurve Python package (Lightkurve Collaboration et al. 2018). For K2 targets, we used the light curves extracted with the EVEREST pipeline (Luger et al. 2016, 2018), which we found to produce light curves with the least noise and systematics for the stars in our sample after a visual comparison. For TESS targets, we used the light curves extracted with the SPOC pipeline (Jenkins et al. 2016) and Quick Look Pipeline (Huang et al. 2020a, 2020b), with a

²⁰ Although we acknowledge that updated catalogs have been published since the original release of the EPIC (e.g., Hardegree-Ullman et al. 2020)

²¹ Yu et al. (2018) reported these as planet candidates with orbital periods of 1.86 and 2.61 days and with transit depths of 1.46% and 0.28%, respectively. However, we note that these candidates were identified in uncalibrated pixels from the K2 mission, meaning they have a higher likelihood of being false positives caused by systematics or background contamination (e.g., Lehmann & Vanderburg 2024).

¹⁸ <https://exofop.ipac.caltech.edu/tess/> (NExSci 2022).

¹⁹ <https://github.com/awmann/metal>

Table 2
Updated Stellar Parameters

ID	T_{eff} (K)	R_{\star} (R_{\odot})	M_{\star} (M_{\odot})	L_{\star} (L_{\odot})	[Fe/H] (dex)	[M/H] (dex)
EPIC 211510580	3359 ± 54	0.356 ± 0.010	0.340 ± 0.020	0.0145 ± 0.0004	-0.044 ± 0.093	-0.078 ± 0.090
EPIC 211663688	3036 ± 54	0.193 ± 0.006	0.160 ± 0.020	0.0028 ± 0.0001	-0.137 ± 0.162	-0.035 ± 0.159
EPIC 211863149	3498 ± 54	0.451 ± 0.013	0.453 ± 0.020	0.0274 ± 0.0007	0.237 ± 0.088	0.146 ± 0.087
EPIC 212048748	3289 ± 50	0.317 ± 0.009	0.293 ± 0.020	0.0106 ± 0.0003	-0.145 ± 0.083	-0.167 ± 0.082
EPIC 212088059	3686 ± 65	0.531 ± 0.015	0.534 ± 0.020	0.0469 ± 0.0019	0.227 ± 0.088	0.177 ± 0.085
EPIC 248433930	3786 ± 58	0.540 ± 0.015	0.536 ± 0.020	0.0540 ± 0.0013	-0.055 ± 0.095	-0.026 ± 0.093
EPIC 248440276	3427 ± 54	0.404 ± 0.011	0.393 ± 0.020	0.0203 ± 0.0006	-0.161 ± 0.085	-0.140 ± 0.084
EPIC 248731669	3700 ± 72	0.534 ± 0.016	0.532 ± 0.021	0.0482 ± 0.0024	-0.027 ± 0.103	-0.020 ± 0.099
EPIC 248775938	3957 ± 69	0.659 ± 0.019	0.635 ± 0.021	0.0958 ± 0.0036	-0.008 ± 0.093	-0.037 ± 0.091
EPIC 248856002	3592 ± 60	0.482 ± 0.014	0.478 ± 0.021	0.0349 ± 0.0012	-0.149 ± 0.092	-0.114 ± 0.089
EPIC 248861279	3761 ± 61	0.556 ± 0.016	0.548 ± 0.020	0.0557 ± 0.0019	-0.153 ± 0.087	-0.116 ± 0.085
TIC 2760710	3075 ± 49	0.243 ± 0.007	0.213 ± 0.020	0.0048 ± 0.0001	0.017 ± 0.093	-0.062 ± 0.089
TIC 415969908	3416 ± 53	0.385 ± 0.011	0.369 ± 0.020	0.0181 ± 0.0004	-0.274 ± 0.086	-0.199 ± 0.084
TIC 12423815	3744 ± 65	0.544 ± 0.016	0.550 ± 0.021	0.0523 ± 0.0020	0.409 ± 0.106	0.279 ± 0.104
TIC 118327550	3398 ± 55	0.409 ± 0.012	0.400 ± 0.021	0.0201 ± 0.0005	-0.083 ± 0.132	-0.052 ± 0.129
TIC 120916706	3402 ± 74	0.452 ± 0.016	0.447 ± 0.022	0.0247 ± 0.0013	-0.115 ± 0.163	-0.037 ± 0.158
TIC 70899085	3903 ± 61	0.591 ± 0.017	0.593 ± 0.020	0.0730 ± 0.0019	0.469 ± 0.084	0.327 ± 0.083
TIC 452866790	3357 ± 52	0.357 ± 0.010	0.339 ± 0.020	0.0145 ± 0.0004	-0.142 ± 0.084	-0.145 ± 0.083
TIC 19025965	4340 ± 70	0.706 ± 0.020	0.673 ± 0.020	0.1591 ± 0.0052	0.144 ± 0.084	0.108 ± 0.083
TIC 348538431	3507 ± 57	0.504 ± 0.014	0.500 ± 0.020	0.0346 ± 0.0011	-0.143 ± 0.087	-0.157 ± 0.085
TIC 318937509	3402 ± 56	0.525 ± 0.015	0.509 ± 0.020	0.0333 ± 0.0011	-0.652 ± 0.105	-0.456 ± 0.101
TIC 218795833	3287 ± 55	0.351 ± 0.010	0.339 ± 0.020	0.0130 ± 0.0005	0.210 ± 0.102	0.105 ± 0.097
TIC 27649847	3472 ± 53	0.420 ± 0.012	0.414 ± 0.020	0.0231 ± 0.0006	-0.016 ± 0.082	-0.037 ± 0.082
TIC 200593988	3557 ± 56	0.474 ± 0.013	0.464 ± 0.020	0.0324 ± 0.0009	-0.422 ± 0.081	-0.306 ± 0.081
TIC 387690507	3735 ± 61	0.531 ± 0.015	0.538 ± 0.020	0.0495 ± 0.0017	0.393 ± 0.096	0.252 ± 0.093
TIC 144700903	3932 ± 61	0.609 ± 0.017	0.607 ± 0.020	0.0800 ± 0.0020	0.459 ± 0.092	0.318 ± 0.090
TIC 237751146	3402 ± 59	0.437 ± 0.013	0.432 ± 0.021	0.0230 ± 0.0009	-0.046 ± 0.101	-0.079 ± 0.097
TIC 50618703	4144 ± 64	0.662 ± 0.018	0.635 ± 0.020	0.1166 ± 0.0032	-0.161 ± 0.083	-0.143 ± 0.082
TIC 192826603	3840 ± 65	0.572 ± 0.016	0.560 ± 0.020	0.0640 ± 0.0023	-0.253 ± 0.103	-0.164 ± 0.101
TIC 170849515	3877 ± 77	0.646 ± 0.020	0.622 ± 0.021	0.0849 ± 0.0044	-0.169 ± 0.137	0.001 ± 0.132
TIC 55488511	3828 ± 60	0.576 ± 0.016	0.564 ± 0.020	0.0641 ± 0.0017	-0.244 ± 0.086	-0.229 ± 0.084
TIC 413248763	3369 ± 56	0.363 ± 0.010	0.346 ± 0.020	0.0153 ± 0.0006	-0.187 ± 0.082	-0.161 ± 0.081
TIC 1133072	3543 ± 59	0.488 ± 0.014	0.496 ± 0.020	0.0339 ± 0.0012	0.385 ± 0.097	0.318 ± 0.095
TIC 296739893	3696 ± 60	0.540 ± 0.015	0.543 ± 0.020	0.0491 ± 0.0015	0.232 ± 0.093	0.176 ± 0.091
TIC 32497972	3904 ± 60	0.600 ± 0.017	0.590 ± 0.020	0.0755 ± 0.0018	0.023 ± 0.089	0.018 ± 0.087
TIC 29960110	3659 ± 73	0.481 ± 0.014	0.478 ± 0.021	0.0374 ± 0.0021	-0.091 ± 0.082	-0.121 ± 0.082
TIC 163539739	3744 ± 59	0.553 ± 0.015	0.545 ± 0.020	0.0541 ± 0.0017	-0.182 ± 0.086	-0.146 ± 0.085
TIC 13684720	3463 ± 54	0.473 ± 0.013	0.475 ± 0.020	0.0290 ± 0.0008	0.193 ± 0.086	0.097 ± 0.084
TIC 343628284	3411 ± 55	0.379 ± 0.011	0.372 ± 0.020	0.0175 ± 0.0005	0.213 ± 0.090	0.133 ± 0.088
TIC 240968774	3676 ± 55	0.498 ± 0.014	0.489 ± 0.020	0.0408 ± 0.0008	-0.334 ± 0.083	-0.295 ± 0.082
TIC 243185500	3475 ± 60	0.369 ± 0.010	0.356 ± 0.020	0.0179 ± 0.0007	0.033 ± 0.088	-0.017 ± 0.087
TIC 201186294	3517 ± 53	0.459 ± 0.013	0.461 ± 0.020	0.0291 ± 0.0007	0.161 ± 0.090	0.122 ± 0.087
TIC 28900646	3533 ± 54	0.458 ± 0.013	0.460 ± 0.020	0.0295 ± 0.0007	0.158 ± 0.082	0.088 ± 0.082
TIC 353475866	3529 ± 56	0.458 ± 0.013	0.459 ± 0.020	0.0293 ± 0.0008	0.154 ± 0.082	0.094 ± 0.081
TIC 470381900	3198 ± 97	0.276 ± 0.008	0.253 ± 0.020	0.0072 ± 0.0008	0.333 ± 0.088	0.233 ± 0.086
TIC 318022259	3699 ± 58	0.532 ± 0.015	0.528 ± 0.020	0.0478 ± 0.0014	-0.083 ± 0.082	-0.066 ± 0.082
TIC 104208182	4041 ± 61	0.658 ± 0.018	0.641 ± 0.020	0.1041 ± 0.0026	0.252 ± 0.085	0.204 ± 0.084
TIC 408636441	3890 ± 70	0.622 ± 0.017	0.610 ± 0.020	0.0799 ± 0.0036	0.108 ± 0.085	0.157 ± 0.084
TIC 389900760	3138 ± 50	0.240 ± 0.007	0.211 ± 0.020	0.0050 ± 0.0001	0.128 ± 0.085	0.047 ± 0.084
TIC 329148988	3574 ± 57	0.458 ± 0.013	0.458 ± 0.020	0.0309 ± 0.0010	0.072 ± 0.083	0.034 ± 0.083
TIC 321688498	3851 ± 61	0.566 ± 0.016	0.560 ± 0.020	0.0634 ± 0.0017	-0.033 ± 0.088	-0.029 ± 0.086
TIC 168751223	3832 ± 65	0.562 ± 0.016	0.562 ± 0.021	0.0614 ± 0.0021	0.218 ± 0.096	0.094 ± 0.095
TIC 212957629	3123 ± 50	0.203 ± 0.006	0.166 ± 0.020	0.0035 ± 0.0001	-0.492 ± 0.088	-0.392 ± 0.087
TIC 330637910	3548 ± 70	0.490 ± 0.015	0.488 ± 0.021	0.0343 ± 0.0017	-0.050 ± 0.102	-0.017 ± 0.100

(This table is available in machine-readable form.)

preference for SPOC data when available due to the shorter cadence of the data and its more careful treatment of spacecraft systematics. Both K2 and TESS light curves can be downloaded on MAST (STScI 2016, 2021). For all light curves, we masked out data flagged as having poor quality and median-

normalized the flux. We then flattened the light curves using the robust spline-fitting Huber-estimator algorithm as implemented in the `wōtan` Python package (Hippke et al. 2019), enforcing a window length (i.e., distance between knots) of 0.5 days. After visually inspecting the light curves using

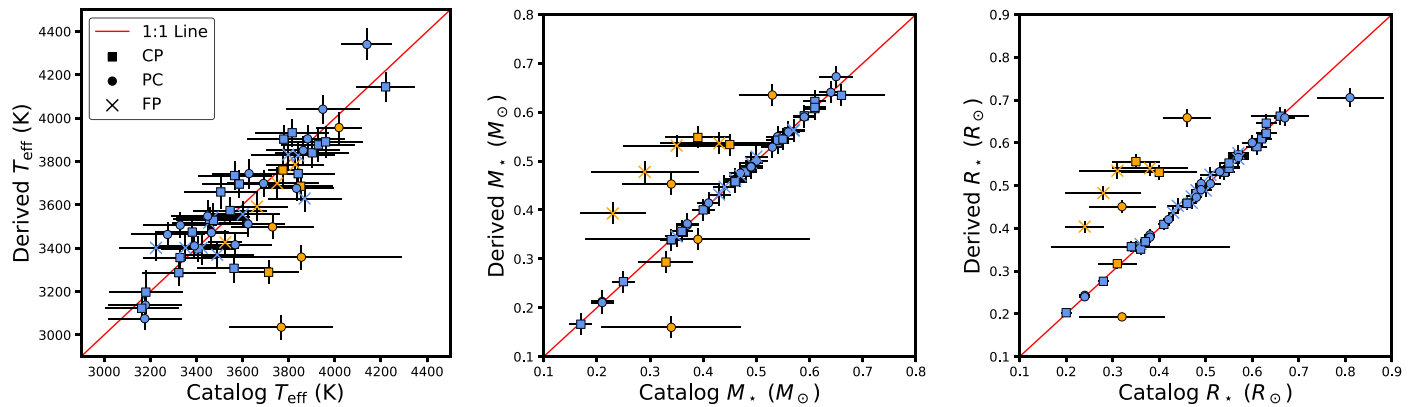


Figure 3. Derived stellar parameters, as discussed in Section 4, plotted against the respective values listed in the EPIC (orange) and the TIC (light blue). Squares indicate stars with at least one confirmed planet, circles indicate stars with only planet candidates, and crosses indicate stars with only false positives or no planet candidates. The solid red line in each panel denotes the 1-to-1 line. In general, our values agree well with the values in the TIC and likely provide improved accuracy over those in the EPIC using stellar models. In many cases, we provide parameters with a greater precision than either catalog.

various knot distances, we determined that this choice does not distort the transit morphologies of the planets and planet candidates analyzed here, which all have transit durations under 3 hr.

5.2. Light-curve Fits

We performed our fits using the `exoplanet` Python package (Foreman-Mackey et al. 2021), which implements the Markov Chain Monte Carlo capabilities of `pymc3` for transiting-planet parameter estimation (Salvatier et al. 2016). For each planet, we began by determining the passband-appropriate quadratic limb-darkening coefficients based on their updated values of $\log g$, T_{eff} , and metallicity (Claret 2017). We initialized each model with the following priors: Gaussian priors on M_* , R_* , and T_{eff} based on the values in Table 2; Gaussian priors on the log of P_{orb} , the log of the planet-star radius ratio (R_p/R_*), and the transit midpoint time (T_0), all centered on the values reported in the literature or on ExoFOP; a uniform prior on the transit impact parameter (b) that ranges from 0 to $1 + R_p/R_*$; and a prior on orbital eccentricity (e) based on Kipping (2013). For each planet and planet candidate, we ran a 10 walker ensemble with 20,000 steps and discarded the first 10,000 steps as burn-in, ensuring convergence using the Gelman–Rubin statistic (Gelman & Rubin 1992). The resulting best-fit parameters are shown in Tables 3 and 4.

6. Discussion

6.1. Updated Planet Radii

A comparison between R_p values derived from our light-curve fits and those listed in the literature are shown in Figure 4. In general, the values derived here agree with those previously found within 1σ uncertainties. However, for a few planets, we derived radii that are discrepant with those listed in the literature at the 1σ level, which can significantly influence our understanding of their bulk densities once their masses are measured.

For one system—TOI-1201 (TIC 29960110)—this can be largely attributed to differences in estimates for R_* . For this star, we calculated $R_* = 0.481 \pm 0.014 R_{\odot}$, whereas Kossakowski et al. (2021) estimates $R_* = 0.508 \pm 0.016 R_{\odot}$. In their calculation, they determined photospheric properties for the host star following Passegger et al. (2019), which involved

comparing a visible wavelength spectrum to a synthetic spectrum, and then determined R_* using the empirical relations in Schweitzer et al. (2019). This difference in techniques is partially responsible for the $\sim 10\%$ difference in measured planet radii.

For three other slightly discrepant systems—TOI-530 (TIC 387690507), TOI-620 (TIC 296739893), and TOI-1468 (TIC 243185500)—we derived stellar radii consistent with those listed in the planet discovery papers at the 1σ level. We attribute the differences in measured planet radii to the fact that more TESS data became available between the publication of those systems and this work, leading to a transit signal that has a higher S/N and is more robust against systematics. Specifically, Gan et al. (2022) did not have access to TESS sectors 44 and 45 for their analysis of TOI-530 b, Reefe et al. (2022) did not have access to TESS sector 62 for their analysis, and Chaturvedi et al. (2022) did not have access to TESS sector 57 for their analysis.

6.2. Stellar Metallicity and System Properties

To assess the reliability of our results and explore trends between derived stellar parameters and system properties, we compared our results to previously characterized low-mass stars from the NASA Exoplanet Archive (NEA) in Figures 5 and 6. We note that only some of the stars from the NEA have properties derived from near-infrared spectra (e.g., Dressing et al. 2019), whereas others have properties derived from photometric relations (e.g., Bonfils et al. 2005; Mann et al. 2013; Kesseli et al. 2019) or isochrone fitting (e.g., Huber et al. 2014; Mathur et al. 2017). Because these properties were not derived in a homogeneous way, there may be systematics present in the data that we do not account for.

Figure 5 separates stars based on planet size. For stars with planets smaller than $4 R_{\oplus}$, we see that small planets are found around low-mass stars with a range of masses and metallicities in both the NEA sample and our sample. One notable feature is that planet-hosting stars seem to be able to have lower [Fe/H] when M_* is relatively high, possibly hinting at a poor planet formation efficiency when both [Fe/H] and M_* are low (Boley et al. 2024). Of the stars in our sample with $M_* < 0.3 M_{\odot}$, the lowest metallicity star hosting a small planet is TIC 212957629 (TOI-2406), with $[\text{Fe}/\text{H}] = -0.492 \pm 0.088$ dex. Of the more massive planet-hosting stars in our sample, TIC 170849515

Table 3
Best-fit Planet Parameters for Confirmed Planets

Name	P_{orb} (days)	T_0 (KBJD or TBJD) ^a	b	a (au)	R_p (R_\oplus)	$R_{\text{p,Lit}}$ (R_\oplus)
K2-313 b	$5.745909^{+0.000035}_{-0.000035}$	$3664.7714^{+0.0022}_{-0.0022}$	$0.58^{+0.11}_{-0.12}$	$0.04170^{+0.00092}_{-0.00091}$	$2.005^{+0.073}_{-0.074}$	$2.025^{+0.096}_{-0.097}$
K2-345 b	$10.367443^{+0.000030}_{-0.000030}$	$2308.7110^{+0.0025}_{-0.0025}$	$0.54^{+0.22}_{-0.27}$	$0.07553^{+0.00094}_{-0.00097}$	$1.99^{+0.12}_{-0.13}$	$2.110^{+0.200}_{-0.009}$
K2-404 b	$13.11372^{+0.00050}_{-0.00050}$	$3084.8388^{+0.0014}_{-0.0014}$	$0.44^{+0.20}_{-0.23}$	$0.0891^{+0.0011}_{-0.0011}$	$2.53^{+0.11}_{-0.11}$	$2.530^{+0.084}_{-0.083}$
TOI-244 b	$7.397216^{+0.000036}_{-0.000036}$	$1357.3625^{+0.0028}_{-0.0028}$	$0.83^{+0.16}_{-0.19}$	$0.05477^{+0.00096}_{-0.00095}$	$1.40^{+0.14}_{-0.17}$	$1.52^{+0.12}_{-0.12}$
TOI-442 b	$4.0520291^{+0.000030}_{-0.000031}$	$2196.11444^{+0.00048}_{-0.00048}$	$0.73^{+0.11}_{-0.11}$	$0.04178^{+0.00048}_{-0.00048}$	$4.66^{+0.23}_{-0.24}$	$4.70^{+0.30}_{-0.30}$
TOI-488 b	$1.1980059^{+0.000019}_{-0.000020}$	$2228.97790^{+0.00086}_{-0.00086}$	$0.25^{+0.19}_{-0.19}$	$0.01538^{+0.00030}_{-0.00030}$	$1.216^{+0.056}_{-0.056}$	$1.264^{+0.050}_{-0.049}$
TOI-519 b	$1.26523285^{+0.0000048}_{-0.0000048}$	$1491.87690^{+0.00023}_{-0.00023}$	$0.22^{+0.11}_{-0.12}$	$0.01599^{+0.00032}_{-0.00032}$	$11.70^{+0.34}_{-0.35}$	$11.50^{+0.30}_{-0.30}$
TOI-530 b	$6.3875854^{+0.000082}_{-0.000084}$	$2530.54083^{+0.00075}_{-0.00077}$	$0.16^{+0.13}_{-0.13}$	$0.05476^{+0.00068}_{-0.00069}$	$8.27^{+0.24}_{-0.24}$	$9.30^{+0.70}_{-0.70}$
TOI-532 b	$2.32684^{+0.0023}_{-0.0023}$	$1470.5758^{+0.0012}_{-0.0012}$	$0.30^{+0.18}_{-0.20}$	$0.02911^{+0.00033}_{-0.00033}$	$5.41^{+0.24}_{-0.24}$	$5.82^{+0.19}_{-0.19}$
TOI-544 b	$1.5483512^{+0.000019}_{-0.000019}$	$1469.75771^{+0.00076}_{-0.00075}$	$0.64^{+0.23}_{-0.31}$	$0.02251^{+0.00024}_{-0.00023}$	$2.14^{+0.14}_{-0.14}$	$2.03^{+0.10}_{-0.10}$
TOI-551 b	$2.6473058^{+0.000025}_{-0.000025}$	$2203.15209^{+0.00062}_{-0.00062}$	$1.03^{+0.11}_{-0.10}$	$0.03089^{+0.00037}_{-0.00037}$	$15.9^{+5.1}_{-4.8}$	$14.9^{+6.8}_{-3.7}$
TOI-555 b	$1.9416425^{+0.000032}_{-0.000032}$	$1438.1464^{+0.0010}_{-0.0011}$	$0.24^{+0.16}_{-0.16}$	$0.02600^{+0.00029}_{-0.00029}$	$11.90^{+0.42}_{-0.42}$	$12.09^{+0.35}_{-0.35}$
TOI-562 b	$3.9305992^{+0.000042}_{-0.000042}$	$2272.67531^{+0.00048}_{-0.00049}$	$0.43^{+0.20}_{-0.24}$	$0.03424^{+0.00067}_{-0.00067}$	$1.233^{+0.047}_{-0.048}$	$1.217^{+0.084}_{-0.083}$
TOI-620 b	$5.0988429^{+0.000055}_{-0.000056}$	$1518.00433^{+0.00064}_{-0.00065}$	$0.65^{+0.24}_{-0.29}$	$0.04732^{+0.00058}_{-0.00058}$	$3.08^{+0.21}_{-0.20}$	$3.76^{+0.15}_{-0.15}$
TOI-1201 b	$2.4919817^{+0.000046}_{-0.000046}$	$1411.6698^{+0.0011}_{-0.0011}$	$0.31^{+0.19}_{-0.20}$	$0.02814^{+0.00040}_{-0.00040}$	$2.183^{+0.087}_{-0.088}$	$2.415^{+0.091}_{-0.090}$
TOI-1278 b	$14.4779^{+0.0024}_{-0.0024}$	$1711.9580^{+0.0018}_{-0.0019}$	$1.030^{+0.086}_{-0.082}$	$0.0950^{+0.0012}_{-0.0012}$	$11.4^{+3.9}_{-3.7}$	$12.2^{+2.7}_{-2.2}$
TOI-1468 b	$1.8805192^{+0.000046}_{-0.000047}$	$2448.30598^{+0.00055}_{-0.00058}$	$0.30^{+0.19}_{-0.20}$	$0.02116^{+0.00039}_{-0.00040}$	$1.398^{+0.056}_{-0.056}$	$1.280^{+0.038}_{-0.039}$
TOI-1468c	$15.532507^{+0.000055}_{-0.000057}$	$2450.35637^{+0.00067}_{-0.00069}$	$0.47^{+0.23}_{-0.27}$	$0.0865^{+0.0016}_{-0.0016}$	$2.005^{+0.089}_{-0.089}$	$2.064^{+0.044}_{-0.044}$
TOI-1634 b	$0.98941^{+0.0011}_{-0.0011}$	$1791.5145^{+0.0016}_{-0.0016}$	$0.30^{+0.19}_{-0.20}$	$0.01503^{+0.00020}_{-0.00021}$	$1.849^{+0.090}_{-0.090}$	$1.790^{+0.080}_{-0.081}$
TOI-1685 b	$0.66916^{+0.0011}_{-0.0011}$	$1816.2247^{+0.0023}_{-0.0024}$	$0.43^{+0.23}_{-0.26}$	$0.01155^{+0.00016}_{-0.00017}$	$1.54^{+0.10}_{-0.10}$	$1.700^{+0.070}_{-0.070}$
TOI-1693 b	$1.7666891^{+0.000048}_{-0.000050}$	$2549.09556^{+0.00098}_{-0.00099}$	$0.24^{+0.20}_{-0.19}$	$0.02205^{+0.00031}_{-0.00032}$	$1.371^{+0.057}_{-0.059}$	$1.41^{+0.10}_{-0.10}$
TOI-1696 b	$2.50052^{+0.00063}_{-0.00063}$	$1816.6980^{+0.0036}_{-0.0036}$	$0.38^{+0.23}_{-0.25}$	$0.02283^{+0.00060}_{-0.00060}$	$3.22^{+0.27}_{-0.29}$	$3.09^{+0.11}_{-0.11}$
TOI-1759 b	$18.85006^{+0.00118}_{-0.00118}$	$2838.7691^{+0.0097}_{-0.0097}$	$0.31^{+0.20}_{-0.21}$	$0.1175^{+0.0013}_{-0.0013}$	$3.33^{+0.13}_{-0.13}$	$3.14^{+0.10}_{-0.10}$
TOI-2285 b	$27.26957^{+0.00097}_{-0.00100}$	$1747.1830^{+0.0051}_{-0.0049}$	$0.58^{+0.23}_{-0.28}$	$0.1367^{+0.0020}_{-0.0020}$	$1.99^{+0.18}_{-0.19}$	$1.740^{+0.080}_{-0.080}$
TOI-2406 b	$3.076673^{+0.000015}_{-0.000015}$	$2475.9470^{+0.0012}_{-0.0012}$	$0.30^{+0.24}_{-0.24}$	$0.02253^{+0.00093}_{-0.00095}$	$2.88^{+0.11}_{-0.16}$	$2.94^{+0.17}_{-0.16}$

Notes. Updated values are medians and 68% confidence intervals of the posterior distributions. The rightmost column contains literature R_p values reported in the following papers: K2-131 b (G 9-40 b; Stefansson et al. 2020), K2-345 b (de Leon et al. 2021), K2-404 b (Zink et al. 2021; Christiansen et al. 2022), TOI-244 b (Castro-González et al. 2023), TOI-442 b (LP 714-47 b; Dreizler et al. 2020), TOI-488 b (GJ 3473b; Kemmer et al. 2020), TOI-519 b (Kagetani et al. 2023, but also see Parviainen et al. 2021), TOI-530 b (Gan et al. 2022), TOI-532 b (Kanodia et al. 2021), TOI-544 b (Giacalone et al. 2022), TOI-551 b (NGTS-1 b; Bayliss et al. 2018), TOI-555 b (HATS-76 b; Jordán et al. 2022), TOI-562 b (GJ 357 b; Luque et al. 2019), TOI-620 b (Reefe et al. 2022), TOI-1201 b (Kossakowski et al. 2021), TOI-1278 b (Artigau et al. 2021), TOI-1468 b and c (Chaturvedi et al. 2022), TOI-1634 b (Cloutier et al. 2021, but also see Hirano et al. 2021), TOI-1685 b (Bluhm et al. 2021, but also see Hirano et al. 2021), TOI-1693 b (Giacalone et al. 2022), TOI-1696 b (Mori et al. 2022, but also see Beard et al. 2022), TOI-1759 b (Espinoza et al. 2022, but also see Martioli et al. 2022), TOI-2285 b (Fukui et al. 2022), and TOI-2406 b (Wells et al. 2021).

^a KBJD applies to K2 targets and is BJD–2454833. TBJD applies to TESS targets and is BJD–2457000.

(This table is available in machine-readable form.)

(TOI-555) and TIC 163539739 (TOI-1278) reach considerably lower metallicities of $[\text{Fe}/\text{H}] = 0.169 \pm 0.137$ dex and $[\text{Fe}/\text{H}] = 0.182 \pm 0.086$ dex, respectively. However, we cannot rule out a sample selection bias as the cause of this apparent trend. Compared to those with small planets, low-mass stars with planets larger than $4 R_\oplus$ appear to occupy a distinctly high- $[\text{Fe}/\text{H}]$ and high- M_\star region of parameter space in both the NEA sample and our sample. However, determining if this tendency is physical would require a more rigorous analysis than we attempt here. Hot Jupiters are known to be rare around stars of nearly all spectral types (e.g., Zhou et al. 2019; Beleznay & Kunimoto 2022; Gan et al. 2023b; Zink et al. 2023), and late M dwarfs are notoriously difficult to search for and confirm planets around due to their low brightnesses at visible wavelengths. Determining if hot Jupiters are truly absent around stars with the lowest masses would require one to assess the search completeness of these stars by Kepler, K2, and TESS. The tendency for giant planets to orbit more metal-rich stars is well known for FGK-type stars (e.g., Fischer & Valenti 2005; Johnson et al. 2010; Sousa et al. 2011), but as of yet this trend has not been

identified for M dwarfs with a high statistical significance (e.g., Gaidos & Mann 2014). Identifying this trend confidently will likely require a large sample of low-mass planet-hosting stars with uniformly derived metallicities.

Figure 6 contains the same stellar sample, but separates the stars based on planet multiplicity. The $[\text{Fe}/\text{H}]$ distributions of the two panels are qualitatively similar, although a slight bias toward lower metallicities appears to be present for the stars with multiple known planets, consistent with the findings of Anderson et al. (2021) and Rodríguez Martínez et al. (2023). However, we again note that this figure contains stars with metallicities derived using a variety of methods, so this apparent tendency may not be significant. We also note that many of the single-planet systems may have additional close-in planets that have yet to be detected, either due to a limited photometric baseline or because the additional planets are nontransiting and the stars have not been monitored with radial velocities. As TESS continues to collect data, and low-mass stars with transiting planets are targeted by radial velocity surveys, the relationship between stellar metallicity and planet multiplicity will likely become clearer.

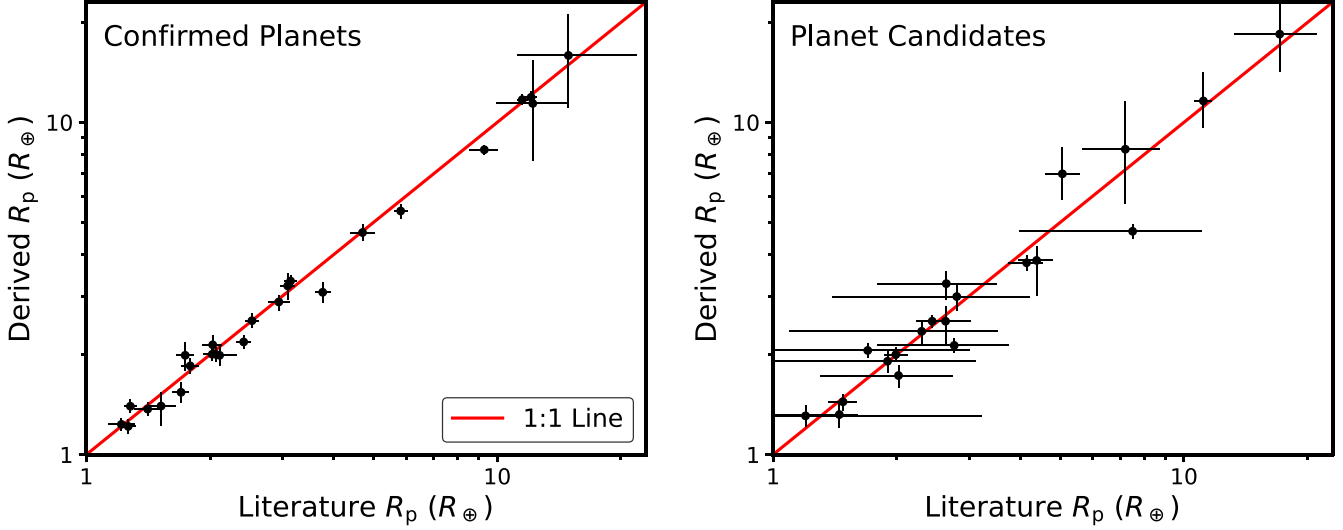


Figure 4. Comparison of planet radii derived in this paper and those previously reported for the confirmed planets in Table 3 (left) and the planet candidates in Table 4 (right).

Table 4
Best-fit Planet Parameters for Planet Candidates

Name	P_{orb} (days)	T_0 (KBJD or TBJD) ^a	b	a (au)	R_p (R_\oplus)	$R_{p,\text{PC}}$ (R_\oplus)
EPIC 211510580.01	$5.31214^{+0.00017}_{-0.00018}$	$2310.1441^{+0.0034}_{-0.0034}$	$0.37^{+0.25}_{-0.26}$	$0.04157^{+0.00083}_{-0.00083}$	$1.32^{+0.11}_{-0.11}$	$1.45^{+0.15}_{-0.96}$
EPIC 248775938.01	$1.753837^{+0.000017}_{-0.000017}$	$3074.84941^{+0.00087}_{-0.00089}$	$0.894^{+0.079}_{-0.042}$	$0.02447^{+0.00028}_{-0.00027}$	$7.0^{+1.4}_{-1.1}$	$5.06^{+0.49}_{-0.44}$
TOI-233.01	$11.670015^{+0.000038}_{-0.000037}$	$1365.2609^{+0.0023}_{-0.0023}$	$0.36^{+0.20}_{-0.22}$	$0.0722^{+0.0013}_{-0.0013}$	$2.058^{+0.094}_{-0.093}$	$1.7^{+1.3}_{-1.3}$
TOI-233.02	$7.201429^{+0.000050}_{-0.000054}$	$1359.4673^{+0.0032}_{-0.0031}$	$0.56^{+0.23}_{-0.28}$	$0.05236^{+0.00094}_{-0.00095}$	$1.73^{+0.12}_{-0.13}$	$2.02^{+0.71}_{-0.71}$
TOI-234.01	$2.8392834^{+0.000059}_{-0.000058}$	$1356.0879^{+0.0012}_{-0.0012}$	$0.73^{+0.22}_{-0.25}$	$0.03215^{+0.00039}_{-0.00039}$	$11.6^{+2.5}_{-1.9}$	$11.15^{+0.50}_{-0.50}$
TOI-493.01	$5.944436^{+0.000011}_{-0.000011}$	$2575.21361^{+0.00083}_{-0.00082}$	$0.51^{+0.20}_{-0.25}$	$0.05628^{+0.00056}_{-0.00055}$	$3.78^{+0.18}_{-0.18}$	$4.14^{+0.38}_{-0.38}$
TOI-507.01	$0.89946587^{+0.0000020}_{-0.0000019}$	$2963.62275^{+0.00082}_{-0.00079}$	$0.94^{+0.13}_{-0.11}$	$0.01446^{+0.00020}_{-0.00020}$	$18.4^{+4.7}_{-4.2}$	$17.1^{+3.8}_{-3.8}$
TOI-521.01	$1.5428486^{+0.0000031}_{-0.0000031}$	$2575.7957^{+0.0010}_{-0.0010}$	$0.28^{+0.22}_{-0.22}$	$0.01947^{+0.00030}_{-0.00031}$	$2.000^{+0.089}_{-0.088}$	$1.99^{+0.12}_{-0.12}$
TOI-557.01	$3.344925^{+0.000016}_{-0.000016}$	$1439.5474^{+0.0023}_{-0.0023}$	$0.66^{+0.21}_{-0.28}$	$0.03617^{+0.00043}_{-0.00043}$	$2.35^{+0.17}_{-0.18}$	$2.3^{+1.2}_{-1.2}$
TOI-876.01	$29.48287^{+0.0027}_{-0.0027}$	$1457.3967^{+0.0051}_{-0.0049}$	$0.75^{+0.18}_{-0.23}$	$0.1567^{+0.0018}_{-0.0018}$	$2.99^{+0.26}_{-0.26}$	$2.8^{+1.4}_{-1.4}$
TOI-1433.01	$12.4379635^{+0.0000066}_{-0.0000064}$	$1695.01136^{+0.00044}_{-0.00080}$	$0.98^{+0.23}_{-0.20}$	$0.0820^{+0.0011}_{-0.0011}$	$27.2^{+8.8}_{-7.5}$	24^{+46}_{-24}
TOI-1448.01	$8.1135^{+0.020}_{-0.020}$	$1713.3338^{+0.0073}_{-0.0073}$	$0.37^{+0.26}_{-0.27}$	$0.0568^{+0.0010}_{-0.0010}$	$3.27^{+0.27}_{-0.33}$	$2.64^{+0.84}_{-0.84}$
TOI-1467.01	$5.9723^{+0.012}_{-0.012}$	$1766.9828^{+0.0046}_{-0.0046}$	$0.51^{+0.23}_{-0.27}$	$0.05077^{+0.00070}_{-0.00070}$	$1.91^{+0.14}_{-0.14}$	$1.9^{+1.2}_{-1.2}$
TOI-1730.01	$6.226124^{+0.000020}_{-0.000020}$	$2603.9611^{+0.0014}_{-0.0014}$	$0.39^{+0.20}_{-0.24}$	$0.05357^{+0.00069}_{-0.00068}$	$2.131^{+0.096}_{-0.096}$	$2.76^{+0.96}_{-0.96}$
TOI-1730.02	$2.1555020^{+0.0000062}_{-0.0000064}$	$2603.3162^{+0.0012}_{-0.0012}$	$0.34^{+0.21}_{-0.22}$	$0.02640^{+0.00034}_{-0.00034}$	$1.442^{+0.077}_{-0.077}$	$1.48^{+0.11}_{-0.11}$
TOI-1730.03	$12.566366^{+0.000038}_{-0.000037}$	$2598.3690^{+0.0010}_{-0.0011}$	$0.23^{+0.20}_{-0.19}$	$0.0855^{+0.0011}_{-0.0011}$	$2.520^{+0.096}_{-0.102}$	$2.44^{+0.11}_{-0.11}$
TOI-1738.01	$3.69759^{+0.0093}_{-0.0090}$	$1792.6603^{+0.0053}_{-0.0059}$	$0.73^{+0.22}_{-0.27}$	$0.04035^{+0.00042}_{-0.00042}$	$3.84^{+0.36}_{-0.82}$	$4.38^{+0.40}_{-0.40}$
TOI-2120.01	$5.799792^{+0.000080}_{-0.000080}$	$1795.8232^{+0.0020}_{-0.0020}$	$0.79^{+0.16}_{-0.18}$	$0.0376^{+0.0012}_{-0.0012}$	$2.52^{+0.26}_{-0.39}$	$2.63^{+0.39}_{-0.39}$
TOI-2290.01	$0.3862296^{+0.0000051}_{-0.0000054}$	$1764.9858^{+0.0020}_{-0.0020}$	$0.44^{+0.25}_{-0.27}$	$0.00855^{+0.00010}_{-0.00010}$	$1.308^{+0.091}_{-0.091}$	$1.2^{+2.0}_{-2.0}$
TOI-2331.01	$4.715073^{+0.000027}_{-0.000027}$	$2167.3349^{+0.0033}_{-0.0033}$	$0.26^{+0.22}_{-0.21}$	$0.04538^{+0.00055}_{-0.00055}$	$4.70^{+0.21}_{-0.22}$	$7.5^{+3.5}_{-3.5}$
TOI-5561.01	$2.00760^{+0.00011}_{-0.00011}$	$2502.1442^{+0.0027}_{-0.0027}$	$0.79^{+0.22}_{-0.20}$	$0.02451^{+0.00037}_{-0.00036}$	$8.3^{+3.2}_{-2.6}$	$7.2^{+1.5}_{-1.5}$

Notes. Updated values are medians and 68% confidence intervals of the posterior distributions. The rightmost column contains the previously reported estimate for R_p . The estimate for EPIC 211510580.01 is from Kruse et al. (2019). The estimate for EPIC 248775938.01 is from Castro González et al. (2020). The estimates for all of the TOIs are from ExoFOP.

^a KBJD (Kepler BJD) applies to K2 targets and is equal to BJD–2454833. TBJD (TESS BJD) applies to TESS targets and is equal to BJD–2457000.

(This table is available in machine-readable form.)

7. Conclusions

We present the results of a survey to collect near-infrared spectra of cool planet-hosting stars with SpeX on the IRTF. We collected spectra of 65 cool stars in order to measure their metallicities and calculate updated stellar parameters. Twenty-five of these stars have confirmed transiting planets and 27 have transiting-planet candidates. Five of our targets host

multiple confirmed planets or multiple planet candidates. The remaining stars either have no planet candidates or previously had planet candidates that have since been determined to be false positives.

Using our metallicities and updated stellar parameters, we performed updated fits of the K2 and TESS light curves to calculate updated properties and orbital parameters of the confirmed planets and planet candidates, finding results in

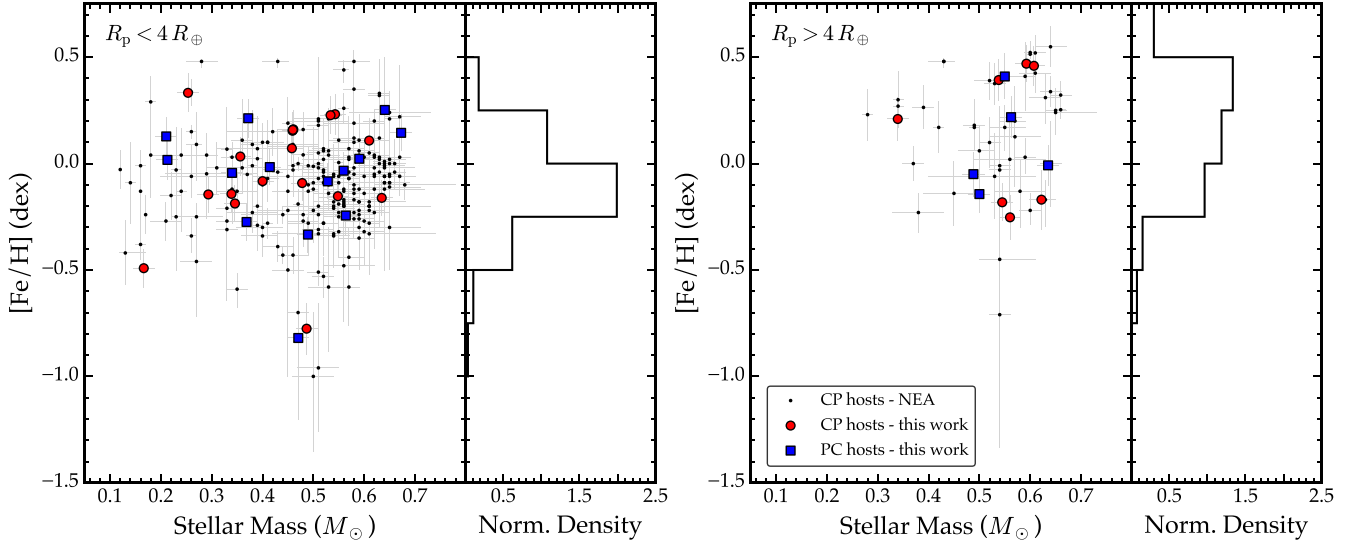


Figure 5. Distribution of stellar masses and metallicities for low-mass stars with at least one small planet ($R_p < 4 R_\oplus$; left) or at least one giant planet ($R_p > 4 R_\oplus$; right). Black dots are the masses and metallicities of stars with $T_{\text{eff}} < 4300$ K, $\log g > 4$, and $M_\star < 0.7 M_\odot$ collected from the NASA Exoplanet Archive, which were calculated using a variety of techniques. Red circles are stars in our sample with at least one confirmed planet. Blue squares are stars in our sample with no confirmed planets but at least one planet candidate. The gray bars are 1σ uncertainties. The histograms on the right of each panel are the normalized density distributions of all points combined. In general, our measured values agree well with previously reported values of similar systems.

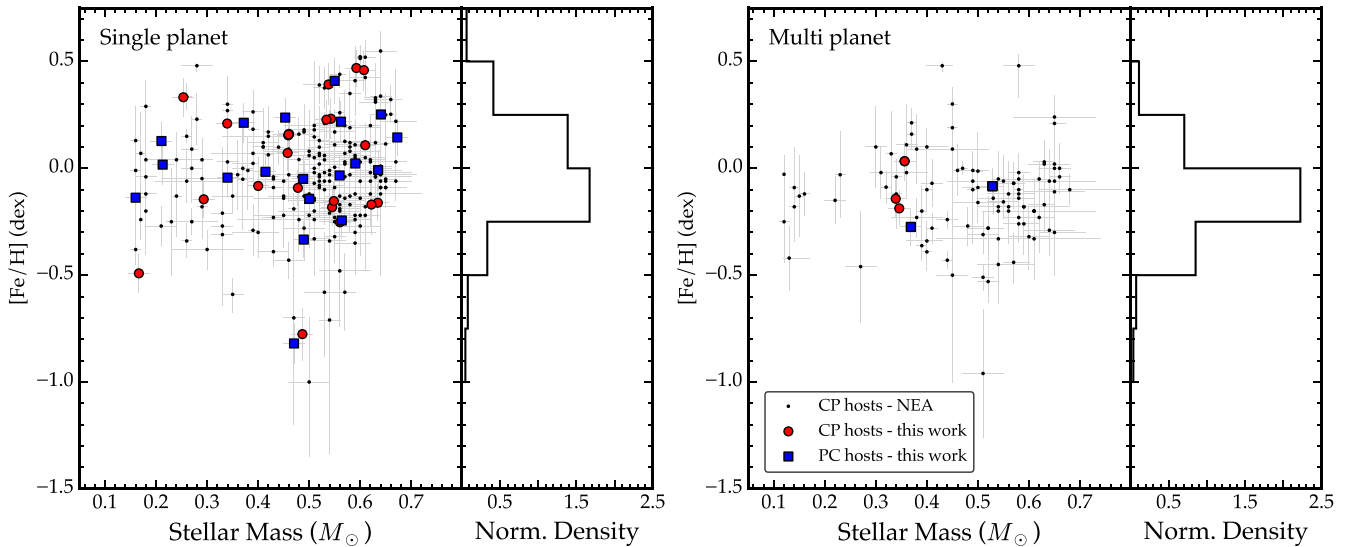


Figure 6. The same as Figure 5, but for systems with only one detected planet or planet candidate (left) and systems with multiple detected planets or planet candidates (right).

general agreement with those reported earlier. We also examine the distribution of planets of different sizes as a function of stellar properties. We found that our derived stellar parameters are consistent with previously studied stars that host similar planetary systems.

Our sample increases the number of planet-hosting M dwarfs and late K dwarfs with spectroscopically determined metallicities. As more planets around cool stars are discovered, these metallicities will enable more rigorous investigations of the correlations between planetary systems and the properties of their low-mass stars.

Acknowledgments

The authors thank Elisabeth R. Newton and Andrew Vanderburg for their constructive feedback on this work and

the telescope proposals associated with the data presented herein.

S.G. is supported by an NSF Astronomy and Astrophysics Postdoctoral Fellowship under award AST-2303922. S.G. and C.D.D. acknowledge support from NASA FINESST award 80NSSC20K1549. C.D.D. and E.T. also acknowledge support provided by the David and Lucile Packard Foundation via grant 2019-69648, the NASA TESS Guest Investigator Program via grant 80NSSC18K1583, and the NASA Exoplanets Research Program (XRP) via grant 80NSSC20K0250. J.Z. acknowledges support provided by NASA through the Hubble Fellowship grant HST-HF2-51497.001 awarded by the Space Telescope Science Institute, which is operated by the Association of Universities for Research in Astronomy, Inc., for NASA, under the contract NAS 5-26555.

This paper includes data collected at the Infrared Telescope Facility, which is operated by the University of Hawaii under contract 80HQTR19D0030 with the National Aeronautics and Space Administration. This research has made use of the NASA Exoplanet Archive, which is operated by the California Institute of Technology, under contract with the National Aeronautics and Space Administration under the Exoplanet Exploration Program. This research has made use of the Exoplanet Follow-up Observation Program (ExoFOP) website, which is operated by the California Institute of Technology, under contract with the National Aeronautics and Space Administration under the Exoplanet Exploration Program.

The Infrared Telescope Facility occupies the summit of Maunakea, a place of significant ecological, cultural, and spiritual importance within the indigenous Hawaiian community. We understand and embrace our accountability to Maunakea and the indigenous Hawaiian community, and commit to our role in long-term mutual stewardship. We are most fortunate to have the opportunity to conduct observations from Maunakea.

Facilities: IRTF, Exoplanet Archive, ExoFOP, MAST.

Software: exoplanet (Foreman-Mackey et al. 2021), Lightkurve (Lightkurve Collaboration et al. 2018), metal (Mann et al. 2013), pymc3 (Salvatier et al. 2016), Spextool (Cushing et al. 2004), tellrv (Newton et al. 2014, 2022), wōtan (Hippke et al. 2019), xtellcor (Vacca et al. 2003).

ORCID iDs

- Rebecca Gore [ID](https://orcid.org/0009-0000-7274-7523) <https://orcid.org/0009-0000-7274-7523>
 Steven Giacalone [ID](https://orcid.org/0000-0002-8965-3969) <https://orcid.org/0000-0002-8965-3969>
 Courtney D. Dressing [ID](https://orcid.org/0000-0001-8189-0233) <https://orcid.org/0000-0001-8189-0233>
 Emma V. Turtelboom [ID](https://orcid.org/0000-0002-1845-2617) <https://orcid.org/0000-0002-1845-2617>
 Charles D. Fortenbach [ID](https://orcid.org/0000-0001-5286-639X) <https://orcid.org/0000-0001-5286-639X>
 Kevin K. Hardegree-Ullman [ID](https://orcid.org/0000-0003-3702-0382) <https://orcid.org/0000-0003-3702-0382>
 Jon K. Zink [ID](https://orcid.org/0000-0003-1848-2063) <https://orcid.org/0000-0003-1848-2063>
 Andrew W. Mayo [ID](https://orcid.org/0000-0002-7216-2135) <https://orcid.org/0000-0002-7216-2135>
 Joshua E. Schlieder [ID](https://orcid.org/0000-0001-5347-7062) <https://orcid.org/0000-0001-5347-7062>
 Jessie L. Christiansen [ID](https://orcid.org/0000-0002-8035-4778) <https://orcid.org/0000-0002-8035-4778>

References

- Anderson, S. G., Dittmann, J. A., Ballard, S., & Bedell, M. 2021, *AJ*, 161, 203
 Artigau, É., Hébrard, G., Cadieux, C., et al. 2021, *AJ*, 162, 144
 Ballard, S. 2019, *AJ*, 157, 113
 Bayliss, D., Gillen, E., Eigmüller, P., et al. 2018, *MNRAS*, 475, 4467
 Bean, J. L., Benedict, G. F., & Endl, M. 2006, *ApJL*, 653, L65
 Beard, C., Robertson, P., Kanodia, S., et al. 2022, *AJ*, 163, 286
 Beleznay, M., & Kunimoto, M. 2022, *MNRAS*, 516, 75
 Belokurov, V., Penoyre, Z., Oh, S., et al. 2020, *MNRAS*, 496, 1922
 Bergsten, G. J., Pascucci, I., Hardegree-Ullman, K. K., et al. 2023, *AJ*, 166, 234
 Bluhm, P., Pallé, E., Molaverdikhani, K., et al. 2021, *A&A*, 650, A78
 Boley, K. M., Christiansen, J. L., Zink, J. K., et al. 2024, AJ, submitted
 Bonfils, X., Delfosse, X., Udry, S., et al. 2005, *A&A*, 442, 635
 Borucki, W. J., Koch, D., Basri, G., et al. 2010, *Sci*, 327, 977
 Boyajian, T. S., von Braun, K., van Belle, G., et al. 2012, *ApJ*, 757, 112
 Brady, M. T., & Bean, J. L. 2022, *AJ*, 163, 255
 Brewer, J. M., Wang, S., Fischer, D. A., & Foreman-Mackey, D. 2018, *ApJL*, 867, L3
 Buchhave, L. A., Bizzarro, M., Latham, D. W., et al. 2014, *Natur*, 509, 593
 Buchhave, L. A., Latham, D. W., Johansen, A., et al. 2012, *Natur*, 486, 375
 Castro González, A., Díez Alonso, E., Menéndez Blanco, J., et al. 2020, *MNRAS*, 499, 5416
 Castro-González, A., Demangeon, O. D. S., Lillo-Box, J., et al. 2023, *A&A*, 675, A52
 Chaturvedi, P., Bluhm, P., Nagel, E., et al. 2022, *A&A*, 666, A155
 Christiansen, J. L., Bhure, S., Zink, J. K., et al. 2022, *AJ*, 163, 244
 Claret, A. 2017, *A&A*, 600, A30
 Cloutier, R., Charbonneau, D., Stassun, K. G., et al. 2021, *AJ*, 162, 79
 Cushing, M. C., Vacca, W. D., & Rayner, J. T. 2004, *PASP*, 116, 362
 de Leon, J. P., Livingston, J., Endl, M., et al. 2021, *MNRAS*, 508, 195
 Dreizler, S., Crossfield, I. J. M., Kossakowski, D., et al. 2020, *A&A*, 644, A127
 Dressing, C. D., & Charbonneau, D. 2013, *ApJ*, 767, 95
 Dressing, C. D., & Charbonneau, D. 2015, *ApJ*, 807, 45
 Dressing, C. D., Hardegree-Ullman, K., Schlieder, J. E., et al. 2019, *AJ*, 158, 87
 Dressing, C. D., Newton, E. R., Schlieder, J. E., et al. 2017, *ApJ*, 836, 167
 El-Badry, K., Rix, H.-W., & Heintz, T. M. 2021, *MNRAS*, 506, 2269
 Espinoza, N., Pallé, E., Kemmer, J., et al. 2022, *AJ*, 163, 133
 ExoFOP 2019, Exoplanet Follow-up Observing Program—TESS, IPAC, doi:10.26134/EXOFOP3
 Fischer, D. A., & Valenti, J. 2005, *ApJ*, 622, 1102
 Foreman-Mackey, D., Luger, R., Agol, E., et al. 2021, *JOSS*, 6, 3285
 Fukui, A., Kimura, T., Hirano, T., et al. 2022, *PASJ*, 74, L1, PASJ
 Gaia Collaboration, Brown, A. G. A., Vallenari, A., et al. 2021, *A&A*, 649, A1
 Gaia Collaboration, Vallenari, A., Brown, A. G. A., et al. 2023, *A&A*, 674, A1
 Gaidos, E., & Mann, A. W. 2014, *ApJ*, 791, 54
 Gaidos, E., Mann, A. W., Kraus, A. L., & Ireland, M. 2016, *MNRAS*, 457, 2877
 Gan, T., Cadieux, C., Jahandar, F., et al. 2023a, *AJ*, 166, 165
 Gan, T., Lin, Z., Wang, S. X., et al. 2022, *MNRAS*, 511, 83
 Gan, T., Wang, S. X., Wang, S., et al. 2023b, *AJ*, 165, 17
 Gelman, A., & Rubin, D. B. 1992, *StaSc*, 7, 457
 Giacalone, S., Dressing, C. D., Hedges, C., et al. 2022, *AJ*, 163, 99
 Girardi, L., Bressan, A., Bertelli, G., & Chiosi, C. 2000, *A&AS*, 141, 371
 Grether, D., & Lineeweaver, C. H. 2006, *ApJ*, 640, 1051
 Hardegree-Ullman, K. K., Cushing, M. C., Muirhead, P. S., & Christiansen, J. L. 2019, *AJ*, 158, 75
 Hardegree-Ullman, K. K., Zink, J. K., Christiansen, J. L., et al. 2020, *ApJS*, 247, 28
 Hartman, J. D., Bakos, G. Á., Csabry, Z., et al. 2023, *AJ*, 166, 163
 Hippke, M., David, T. J., Mulders, G. D., & Heller, R. 2019, *AJ*, 158, 143
 Hirano, T., Livingston, J. H., Fukui, A., et al. 2021, *AJ*, 162, 161
 Hobson, M. J., Jofré, E., García, L., Petrucci, R., & Gómez, M. 2018, *RMxAA*, 54, 65
 Howell, S. B., Sobeck, C., Haas, M., et al. 2014, *PASP*, 126, 398
 Huang, C. X., Vanderburg, A., Pál, A., et al. 2020a, *RNAAS*, 4, 204
 Huang, C. X., Vanderburg, A., Pál, A., et al. 2020b, *RNAAS*, 4, 206
 Huber, D., Bryson, S. T., Haas, M. R., et al. 2016, *ApJS*, 224, 2
 Huber, D., Silva Aguirre, V., Matthews, J. M., et al. 2014, *ApJS*, 211, 2
 Jenkins, J. M., Twicken, J. D., McCauliff, S., et al. 2016, *Proc. SPIE*, 9913, 9913E
 Johnson, J. A., Aller, K. M., Howard, A. W., & Crepp, J. R. 2010, *PASP*, 122, 905
 Johnson, J. A., & Apps, K. 2009, *ApJ*, 699, 933
 Jordán, A., Hartman, J. D., Bayliss, D., et al. 2022, *AJ*, 163, 125
 Kagetani, T., Narita, N., Kimura, T., et al. 2023, *PASP*, 75, 713
 Kanodia, S., Stefansson, G., Cañas, C. I., et al. 2021, *AJ*, 162, 135
 Kemmer, J., Stock, S., Kossakowski, D., et al. 2020, *A&A*, 642, A236
 Kesseli, A. Y., Kirkpatrick, J. D., Fajardo-Acosta, S. B., et al. 2019, *AJ*, 157, 63
 Kipping, D. M. 2013, *MNRAS*, 434, L51
 Kossakowski, D., Kemmer, J., Bluhm, P., et al. 2021, *A&A*, 656, A124
 Kruse, E., Agol, E., Luger, R., & Foreman-Mackey, D. 2019, *ApJS*, 244, 11
 Kunimoto, M., Winn, J., Ricker, G. R., & Vanderspek, R. K. 2022, *AJ*, 163, 290
 Lehmann, D. A., & Vanderburg, A. 2024, arXiv:2402.07903
 Lightkurve Collaboration, Cardoso, J. V. D. M., Hedges, C., et al. 2018, Lightkurve: Kepler and TESS time series analysis in Python, *Astrophysics Source Code Library*, ascl:1812.013
 Lindegren, L., Hernández, J., Bombrun, A., et al. 2018, *A&A*, 616, A2
 Luger, R., Agol, E., Kruse, E., et al. 2016, *AJ*, 152, 100
 Luger, R., Kruse, E., Foreman-Mackey, D., Agol, E., & Saunders, N. 2018, *AJ*, 156, 99
 Luque, R., Pallé, E., Kossakowski, D., et al. 2019, *A&A*, 628, A39
 Maldonado, J., Micela, G., Baratella, M., et al. 2020, *A&A*, 644, A68

- Mann, A. W., Brewer, J. M., Gaidos, E., Lépine, S., & Hilton, E. J. 2013, *AJ*, **145**, 52
- Mann, A. W., Deacon, N. R., Gaidos, E., et al. 2014, *AJ*, **147**, 160
- Mann, A. W., Dupuy, T., Kraus, A. L., et al. 2019, *ApJ*, **871**, 63
- Mann, A. W., Feiden, G. A., Gaidos, E., Boyajian, T., & von Braun, K. 2015, *ApJ*, **804**, 64
- Mann, A. W., Gaidos, E., Lépine, S., & Hilton, E. J. 2012, *ApJ*, **753**, 90
- Marigo, P., & Girardi, L. 2007, *A&A*, **469**, 239
- Marigo, P., Girardi, L., Bressan, A., et al. 2008, *A&A*, **482**, 883
- Martinez, A. O., Crossfield, I. J. M., Schlieder, J. E., et al. 2017, *ApJ*, **837**, 72
- Martioli, E., Hébrard, G., Fouqué, P., et al. 2022, *A&A*, **660**, A86
- Mathur, S., Huber, D., Batalha, N. M., et al. 2017, *ApJS*, **229**, 30
- Mori, M., Livingston, J. H., Leon, J. D., et al. 2022, *AJ*, **163**, 298
- Morton, T. D., Bryson, S. T., Coughlin, J. L., et al. 2016, *ApJ*, **822**, 86
- Muirhead, P. S., Dressing, C. D., Mann, A. W., et al. 2018, *AJ*, **155**, 180
- Muirhead, P. S., Mann, A. W., Vanderburg, A., et al. 2015, *ApJ*, **801**, 18
- Mulders, G. D., Pascucci, I., Apai, D., Frasca, A., & Molenda-Žakowicz, J. 2016, *AJ*, **152**, 187
- Mulders, G. D., Pascucci, I., & Apai, D. 2015, *ApJ*, **798**, 112
- NASA Exoplanet Science Institute 2020, Planetary Systems Table, IPAC, doi:[10.26133/NEA12](https://doi.org/10.26133/NEA12)
- Neves, V., Bonfils, X., Santos, N. C., et al. 2013, *A&A*, **551**, A36
- Newton, E. R., Charbonneau, D., Irwin, J., & Mann, A. W. 2015, *ApJ*, **800**, 85
- Newton, E. R., Charbonneau, D., Irwin, J., et al. 2014, *AJ*, **147**, 20
- Newton, E. R., Charbonneau, D., Irwin, J., et al. 2022, tellrv: Radial velocities for low-resolution NIR spectra, Astrophysics Source Code Library, ascl:[2201.007](https://doi.org/10.2201/007)
- NExScI 2022, Exoplanet Follow-up Observing Program Web Service, IPAC, doi:[10.26134/EXOFOPS](https://doi.org/10.26134/EXOFOPS)
- Parviainen, H., Palle, E., Zapatero-Osorio, M. R., et al. 2021, *A&A*, **645**, A16
- Passegger, V. M., Schweitzer, A., Shulyak, D., et al. 2019, *A&A*, **627**, A161
- Petigura, E. A., Marcy, G. W., Winn, J. N., et al. 2018, *AJ*, **155**, 89
- Rains, A. D., Žerjal, M., Ireland, M. J., et al. 2021, *MNRAS*, **504**, 5788
- Rayner, J. T., Cushing, M. C., & Vacca, W. D. 2009, *ApJS*, **185**, 289
- Rayner, J. T., Onaka, P. M., Cushing, M. C., & Vacca, W. D. 2004, *Proc. SPIE*, **5492**, 1498
- Rayner, J. T., Toomey, D. W., Onaka, P. M., et al. 2003, *PASP*, **115**, 362
- Reefe, M. A., Luque, R., Gaidos, E., et al. 2022, *AJ*, **163**, 269
- Ricker, G. R., Winn, J. N., Vanderspek, R., et al. 2015, *JATIS*, **1**, 014003
- Rodríguez Martínez, R., Martín, D. V., Gaudi, B. S., et al. 2023, *AJ*, **166**, 137
- Rojas-Ayala, B., Covey, K. R., Muirhead, P. S., & Lloyd, J. P. 2012, *ApJ*, **748**, 93
- Sahlmann, J., Ségransan, D., Queloz, D., et al. 2011, *A&A*, **525**, A95
- Salvatier, J., Wiecki, T., & Fonnesbeck, C. 2016, *PeerJ Comput. Sci.*, **2**, e55
- Schweitzer, A., Passegger, V. M., Cifuentes, C., et al. 2019, *A&A*, **625**, A68
- Sharma, S., Bland-Hawthorn, J., Johnston, K. V., & Binney, J. 2011, *ApJ*, **730**, 3
- Skrutskie, M. F., Cutri, R. M., Stiening, R., et al. 2006, *AJ*, **131**, 1163
- Sousa, S. G., Santos, N. C., Israelian, G., Mayor, M., & Udry, S. 2011, *A&A*, **533**, A141
- Stassun, K. G., Oelkers, R. J., Paegert, M., et al. 2019, *AJ*, **158**, 138
- Stassun, K. G., Oelkers, R. J., Pepper, J., et al. 2018, *AJ*, **156**, 102
- Stefansson, G., Cañas, C., Wisniewski, J., et al. 2020, *AJ*, **159**, 100
- STScI 2016, K2 Light Curves (all), MAST, doi:[10.17909/T9WS3R](https://doi.org/10.17909/T9WS3R)
- STScI 2021, TESS Light Curves—All Sectors, MAST, doi:[10.17909/t9-nmc8-f686](https://doi.org/10.17909/t9-nmc8-f686)
- Terrien, R. C., Mahadevan, S., Bender, C. F., et al. 2012, *ApJL*, **747**, L38
- Terrien, R. C., Mahadevan, S., Deshpande, R., & Bender, C. F. 2015, *ApJS*, **220**, 16
- Vacca, W. D., Cushing, M. C., & Rayner, J. T. 2003, *PASP*, **115**, 389
- Weiss, L. M., Isaacson, H. T., Marcy, G. W., et al. 2018, *AJ*, **156**, 254
- Wells, R. D., Rackham, B. V., Schanche, N., et al. 2021, *A&A*, **653**, A97
- Wittenmyer, R. A., Sharma, S., Stello, D., et al. 2018, *AJ*, **155**, 84
- Yu, L., Crossfield, I. J. M., Schlieder, J. E., et al. 2018, *AJ*, **156**, 22
- Zhou, G., Huang, C. X., Bakos, G. Á., et al. 2019, *AJ*, **158**, 141
- Zink, J. K., Hardegree-Ullman, K. K., Christiansen, J. L., et al. 2021, *AJ*, **162**, 259
- Zink, J. K., Hardegree-Ullman, K. K., Christiansen, J. L., et al. 2023, *AJ*, **165**, 262